Localization of Mutant Huntingtin with HTT Exon1 P90 C-terminal Neoepitope Antibodies in Relation to Regional and Neuronal Vulnerability in Forebrain in Q175 Mice and Human Huntington's Disease

Running Title: Mutant exon 1 huntingtin localization

By

Yunping Deng, Marion Joni, Hongbing Wang, Rachel Cox, and Anton Reiner

Department of Anatomy and Neurobiology, The University of Tennessee Health Science Center, Memphis, TN 38163

Corresponding Author: Dr. Anton Reiner
Department of Anatomy & Neurobiology
University of Tennessee Health Science Center
855 Monroe Ave.
Memphis, TN 38163
office: 901-448-8298
fax: 901-448-7193
e-mail: areiner@uthsc.edu

Abstract

Background
Recent evidence suggests that accumulation of mutant exon 1 protein may be critical to HD pathogenesis, but the relation of this to differential regional and cellular vulnerability in HD is unknown.

Objective
We assessed the contribution of the accumulation of the mutant huntingtin exon 1 protein to the regional and cellular variation in HD brain pathology by determining if more vulnerable regions and neuron types were relatively enriched.

Methods
We performed immunolabeling using the novel monoclonal antibodies 11G2 and 1B12 against the C-terminal proline 90 (P90) neoepitope of the huntingtin exon 1 protein on forebrain of Q175 mice and human HD cases, which detect accumulation of monomeric, oligomeric and aggregates mutant exon 1 protein.

Results
Diffuse nuclear and aggregate immunolabeling increased in abundance in Q175 with age, with striatal projection neurons showing immunolabeling earlier than cortical neurons, and pallidal regions only showing neuropil immunolabeling. Nonetheless, some regions less affected in HD, such as hippocampus, were rich in mutant exon 1 protein as well. In humans, striatal immunolabeling was sparser than in mouse, and mainly in the neuropil, but less sparse than in striatal target areas. In human HD cortex, the P90 antibodies detected predominantly neuropil aggregates, which appeared to, in part, localize to dendrites.

Conclusions
Our results indicate that exon 1 mutant protein burden does appear to partly account for overall forebrain vulnerability in HD, but additional factors may contribute to vulnerability differences among forebrain regions and between specific neuron types.

Key Words: pathogenesis, mutant exon 1 protein, basal ganglia, immunohistochemistry,

regional vulnerability,

Introduction

Although the greatest atrophy and neuron loss occurs within the striatal part of the basal ganglia in Huntington's disease (HD) (Deng et al., 2004; Reiner et al., 2011), substantial atrophy and neuron loss also occur in the pallidal part of the basal ganglia, as well as in the cerebral cortex (Reiner et al., 2011). Within striatum, striatal projection neurons (SPNs) are much more vulnerable than are cholinergic interneurons (Albin et al., 1990; Reiner et al., 2011; Reiner and Deng, 2018). SPNs are, however, not all alike in their vulnerability, since enkephalinergic indirect pathway SPNs (iSPNs) projecting to globus pallidus externus (GPe) show greater loss during HD than substance P-containing direct pathway SPNs (dSPNs) projecting to globus pallidus internus (GPi) (Reiner et al., 1988; Sapp et al., 1993; Glass et al., 2000; Deng et al., 2004; Reiner and Deng, 2018). In contrast to cholinergic interneurons, GABAergic interneurons containing parvalbumin (PARV) are as vulnerable as iSPNs (Reiner et al., 2011, 2013).

The basis of the greater vulnerability of some neuron types in striatum, and the overall regional heterogeneity in HD pathology, has been uncertain, but one possibility is that it is related to heterogeneity in the production and accumulation of mutant protein (Wang et al., 2008). Surprisingly, however, prior studies have found mutant protein aggregates in only a small percent of striatal neurons in human HD patients (DiFiglia et al., 1997; Maat-Schieman et al., 1999; Kuemmerle et al., 1999), despite their prominence in striatal neurons in mouse models of HD (Davies et al., 1997; Meade et al., 2002; Brooks and Dunnett, 2015). Recent evidence has accrued that mutant huntingtin toxicity seems to occur due to production of a mutant exon 1 protein stemming from a CAG-dependent splicing failure during the processing of immature mutant huntingtin transcripts, with this propensity increasing as the CAG repeat expands (Sathasivam et al., 2013; Neueder et al., 2017). This has focused attention on the accumulation

of the mutant exon 1 protein and the relationship of that accumulation to differential regional and cellular vulnerability in HD.

Our present immunolabeling study reports on the first use of recently generated antibodies directed against the C-terminal neoepitope at proline 90 (P90 based on polyQ 23 numbering) of the exon 1 huntingtin (HTT) protein, namely the P90 monoclonal antibody clones 11G2 and 1B12 (Missineo et al., 2024), to characterize the forebrain distribution of mutant exon 1 protein in human HD brain and in the Q175 mouse (Heikkinen et al., 2012; Menalled et al., 2012; Deng et al., 2021), which like in human produces mutant exon 1 protein (Franich et al., 2019; Smith et al., 2023). We relate our findings to differential regional vulnerability in HD (Reiner et al., 2011; Reiner and Deng, 2018), and find that exon 1 mutant protein burden is consistent with some aspects of differential forebrain vulnerability in HD, but additional factors may contribute to vulnerability differences among non-basal ganglia forebrain regions and between specific neuron types in HD.

Materials and Methods

Anti-Huntingtin Antibodies Used. The antibodies referred to as "P90 antibodies", specifically clones 11G2 and 1B12, are rabbit monoclonal antibodies raised against the C-terminal 8 amino acids (AEEPLHRP-OH) of the human exon 1 protein with a free carboxylate at P90 (numbering based on 23Q) (Table 1). The specificity for the C-terminal neoepitope of exon 1 was shown by surface plasmon resonance (SPR), western blotting, ELISA, and dot blotting with counter-screening against longer and shorter HTT peptides, N-terminal HTT fragments, and full length recombinant HTT (Missineo et al., 2024). We also assessed the relationship of the mutant exon 1 protein detection with the P90 antibodies to those with the PHP1 and MW8

antibodies. PHP1 was generated against a recombinant HTT Exon1 (20Q) GST-fusion protein and detects a polyproline region of the exon 1 protein (Table 1) (Ko et al., 2018). MW8 antibody was generated against an aggregated form of recombinant human exon 1 (67Q) protein and was shown by peptide array epitope mapping (dot blot) to recognize the sequence AEEPLHRP (Table 1), with recognition not found to be ablated by addition of amino acids to the C-terminus of Exon 1 (Ko et al., 2001), suggesting MW8 is not selective for the exon 1 protein. Landles et al. (2010) later reported, by contrast, that although MW8 does recognize the epitope AEEPLHRP, it does not do so in the context of longer fragments, based on western blot studies of over-expressed N-terminal HTT fragments of varying length. Consistent with the interpretation that MW8 is, in fact, selective for exon 1 huntingtin protein, Smith et al. (2023) reported that MW8 does not detect a signal in the brains of N171-82Q transgenic mice, which cannot produce exon 1 protein from their mutant HD transgene.

Mouse Studies - Subjects. Heterozygous male Q175 HD and wildtype (WT) littermate mice were obtained from JAX at approximately 2, 6, 12, and 18 months of age (Bar Harbor, ME). The CAG repeat length was assessed by the Laragen Corporation (Culver City, CA) and found to be about 190. By convention, these HD mutant mice are nonetheless referred to as Q175 mice (Menalled et al., 2014). We also performed immunolabeling studies on tissues from N171-82Q mice, and huntingtin-flox mice with a tamoxifen inducible Cre recombinase (Httflox/flox;CAG-CreERT). N171-82Q mice were examined at 4 months of age, when they are symptomatic and feature abundant mutant protein aggregates in brain (Schilling et al., 1999). These mice were bred at Johns Hopkins University, and shipped to us as fixed whole brain by Dr. Wenzhen Duan. The Httflox/flox;CAG-CreERT mice were 3 months old and one month post vehicle or tamoxifen treatment (Bragg et al., 2024). These mice were prepared at the

University of Washington, and shipped to us as fixed whole brain by Dr. Jeff Carroll. All animal use was carried out in accordance with the National Institutes of Health Guide for Care and Use of Laboratory Animals and Society for Neuroscience Guidelines, and with the approval of the University of Tennessee Health Science Center Animal Care and Use Committee (approval 21-0308) on November 8, 2021.

Mouse Studies – Immunohistochemical Methods. Immunohistochemical studies in mice were carried out on paraformaldehyde-fixed tissue (Deng et al., 2021). The localization in Q175 mouse brain focused on mutant huntingtin load in basal ganglia and related regions (i.e., substantia nigra and subthalamic nucleus), as well as in pallial structures of the telencephalon (which include cerebral cortex, hippocampus, and amygdala), and thalamus and hypothalamus. The studies in N171-82Q and Httflox/flox;CAG-CreERT mice evaluated P90 antibody specificity. The species host, source, immunogen and specificity of each of the primary antibodies used to detect mutant huntingtin, and all others used as described below, are shown in Table 1. Note that specificity of all antibodies used was confirmed by the source, or by us in prior studies (Deng et al., 2021; Dragatsis et al., 2018).

For these studies, mice were deeply anesthetized, and perfused transcardially with paraformaldehyde fixative and sectioned frozen on a sliding microtome as described previously (Deng et al., 2021). To evaluate the regional distribution of 11G2 and 1B12 labeling, the peroxidase-antiperoxidase (PAP) procedure using diaminobenzidine (DAB) as the chromogen was employed to immunolabel sections, as described previously (Meade et al., 2002; Reiner et al., 2007; Dragatsis et al., 2009; Deng et al., 2021). Sections were then mounted onto gelatin-coated slides, dried, cleared and coverslipped with Permount®. Mapping was conducted using high-resolution, uniformly illuminated digital images of the immunolabeled sections acquired

using a digital scanner (3DHistech KFT Pannoramic 250 Flash scanner), supplemented by microscopic examination of sections. To assess the localization of P90 signal relative to the expression of WT huntingtin, we used the D7F7 rabbit monoclonal antibody against human huntingtin (Cell Signalling) and PAP immunolabeling.

To assess the cell-type specific localization of 11G2 signal, we used immunofluorescence co-labeling for markers of striatal and/or cortical neuron types. To identify neurons per se, we either used NeuroTrace 435/455 (ThermoFisher) as a general counterstain (1:100), or immunolabeling using a mouse monoclonal anti-NeuN (Chemicon) (1:2500). Cholinergic striatal interneurons were visualized by immunolabeling (1:100) for choline acetyltransferase (ChAT) using a goat polyclonal antibody (Millipore), and parvalbuminergic interneurons were visualized by immunolabeling (1:5000 dilution) using a mouse monoclonal anti-PARV (Sigma-Aldrich). To assess the relative abundance of 11G2 signal in the two types of SPNs, we used a rat monoclonal antibody against the D1 dopamine receptor (Sigma-Aldrich) to distinguish dSPNs (D1-rich) from iSPNs (D1-poor). To assess the localization of mutant protein aggregates to dendrites in cerebral cortex, we combined 11G2 immunofluoresence with labeling using the SMI32 mouse monoclonal antibody (Abcam) (Thu et al., 2010; Nana et al., 2014). Secondaries conjugated to distinct Alexa fluorophores raised in compatible species (goat or donkey) and directed against appropriate species IgG were used to differentiate the various immunofluoresence markers, as in our prior studies (Meade et al., 2002; Reiner et al., 2007; Dragatsis et al., 2009; Deng et al., 2021). Finally, we used multiple immunofluorescence and confocal laser-scanning microscopy (CLSM) to assess the colocalization of 11G2, PHP1 and MW8. Although both raised in mouse, PHP1 and MW8 could be selectively detected by different secondary antibodies because they differ in their IgG subtype (Table 1). A Zeiss 710

confocal laser-scanning microscope (Carl Zeiss AG, Oberkochen, Germany) was used to collect images of the immunofluorescence tissue. CLSM images shown here were adjusted for brightness, contrast and sharpness with Photoshop, always processing image groups correspondingly.

Microscopic Analysis in Mouse – 11G2 Regional Scoring. We scored the regional abundance of 11G2 signal in basal ganglia and other forebrain structures at 2, 6, 12 and 18 months of age in Q175 mice on a 5-point scale, with 0 indicating no labeling and 4 indicating extremely pervasive labeling. Several cases per age were analyzed and scored, for which the DAB-immunolabeled tissue was used. The scoring system is based on the regional density of 11G2+ immunolabeling, with a score of 1 denoting moderate diffuse perikaryal labeling, a score of 2 denoting more intense diffuse perikaryal labeling with some small 11G2+ aggregates, a score of 3 denoting numerous, a moderate density of perikaryal and neuropil aggregates, and a score of 4 denoting a high density of perikaryal and neuropil aggregates. For any given region, the labeling generally progressed from initially diffuse perikaryal only to aggregate labeling superseding the diffuse labeling with advancing age.

Microscopic Analysis in Mouse – 11G2 Quantification in SPNs. Striatum in NeuroTrace-stained sections from mutant mice that had been immunolabeled for 11G2 in combination with D1 were analyzed for diffuse and aggregated mutant protein load at 6 and 18 months of age in Q175 mice. For each mutant mouse, CLSM images of dorsolateral striatum were captured using a 40x objective, and the load per D1-rich versus D1-poor neuron types determined using NIH ImageJ. In our approach, the NeuN/NeuroTrace signal was used to create a mask of individual striatal perikarya (excluding those in the size range of cholinergic neurons), and the mask was subsequently directed to the D1 and 11G2 channels to measure the area

occupied for each cell body by thresholded D1 signal and thresholded 11G2 signal, respectively. This approach for analyzing signal in multiple channels is similar to that used by us in Honig et al. (2021). We regarded the more D1-enriched half of the total striatal population analyzed as dSPNs, and the more D1-poor half of the total striatal population analyzed as iSPNs. For comparison of the two SPN types, t-tests were performed, using Excel.

Humans Studies - Subjects. Immunolabeling, imaging, and analysis were performed in human tissue as in our prior studies (Deng et al., 2004; Reiner et al., 2013; Reiner et al., 2012; Deng et al., 2021). Coronal tissue blocks containing caudate and putamen at a rostral level and/or at a level through globus pallidus (GP), blocks containing substantia nigra, blocks containing hippocampus, and blocks containing several different cortical gyri were obtained for 22 HD cases (male=11, female=11) that were verified by pathology, symptoms, family history, and/or CAG repeat (Table 2). All human studies were conducted on de-identified postmortem tissue, and thus the University of Tennessee Health Science Center Institutional Review Board waived the requirement for approval (16-04430-NHSR). The cortical areas we focused on were Brodmann's areas A9 and A46 (frontal cortex), area A4 (primary motor cortex), A6 (premotor cortex), A13-16 (insular cortex), area A7 (posterior parietal cortex), and A22 (superior temporal cortex). The tissues were obtained from the University of Tennessee Health Science Center (UTHSC), the University of Michigan Medical Center (Ann Arbor, MI), the National Neurological Resource Bank (NNRB, Los Angeles, CA), the Douglas Hospital Research Center (DHRC, Montreal, Canada), the University of Rochester (UR), and the Alabama Brain Collection of the University of Alabama at Birmingham (UAB). Brains were immersion-fixed in formalin after autopsy. HD cases were staged according to Vonsattel et al. (1985).

Immunohistochemical Methods in Human. Tissue blocks for HD and/or control cases were transferred to 20% sucrose/10% glycerol/0.1M sodium phosphate buffer (PB) (pH 7.4). Frozen sections were cut at 80 µm with a sliding microtome, and then processed by immunohistochemistry. To enhance immunolabeling, sections were immersed for 30 min in 1% sodium borohydride in PB, 0.1 M DL-lysine in PB, followed by 0.2% nonfat dry milk in PB. We additionally used antigen retrieval methods as described in our prior studies (Jiao et al., 1999; Richfield et al., 2002; Deng et al., 2004). The primary antibodies and immunolabeling methods were as for mouse, with 1% bovine serum albumin added (Deng et al., 2004; Reiner et al., 2013). The free-floating sliding microtome sections were incubated in microcentrifuge vials for 48–72 h at 4°C. After incubation in primary antibody, a set of sections from each case was processed by the peroxidase-antiperoxidase (PAP) method, followed by visualization with DAB, for mapping purposes. The immunolabeled sections were mounted onto gelatin-coated slides, dried, cleared and coverslipped with Permount®. We also used multiple immunofluorescence and CLSM to assess the colocalization of 11G2, PHP1 and MW8, using the same immunolabeling methods as in mouse, as well as to examine the colocalization of 11G2 with SMI32. Sudan Black B treatment was used to suppress autofluorescence in human brains by incubation of slide-mounted sections in 0.3% Sudan Black B for 10 minutes, followed by rinsing in TBS prior to coverslipping. In all immunofluorescence cases, the sections were counterstained with NeuroTrace (1:100) for cytoarchitectonic detail. As in mouse, we scored the regional abundance of 11G2 in basal ganglia structures (somatic and limbic both) and other forebrain structures on a 5-point scale, with 0 indicating no labeling and 4 indicating extremely pervasive labeling, using the PAP/DAB-immunolabeled tissue.

Results

P90 Labeling in Q175 Mouse Basal Ganglia and Related Structures. Both the 11G2 and 1B12 antibodies (more so 11G2) detected mutant huntingtin exon 1 accumulation in 2-, 6-, 10-, 12-, and 18-month old Q175 mice (Fig. 1B-D, F-H). At 2 months of age, we observed diffuse nuclear P90 immunolabeling in the vast majority of neurons in both somatic striatum (caudate-putamen) and limbic striatum (nucleus accumbens and olfactory tubercle), and thus the vast majority of SPNs (Fig. 1F-H), as also reported by Smith et al. (2023) using the S830 antibody. In the older Q175 mice, we additionally detected neuropil and nuclear aggregates, and gradually lessened diffuse nuclear labeling in striatum. The nuclear and neuropil aggregates increased in size and abundance with age. The diffuse nuclear labeling appeared granular at higher magnification viewing, and the lessened diffuse labeling likely reflects the coalescence of the diffusely localized antigen into aggregates. Neurons in GPe, GPi, SNr and ventral pallidum were rarely labeled by the P90 antibodies. Rather, neuropil aggregates gradually increased in frequency in these SPN target areas as the mutant mice aged. Nuclear 11G2 and 1B12 immunolabeling was seen in a minority of subthalamic nucleus (STN) cell bodies. Of note, we saw immunolabeling in Q175 WT mice (Fig. 1A, E), as well as in 2-month Q175 mice (Fig. 1B), that resembled what we have seen with antibodies against WT huntingtin (Fusco et al., 1999; Dragatsis et al., 2018) – namely immunolabeling of the perikaryal cytoplasm of presumptive cholinergic striatal interneurons, and of presumptive SPN terminals in GPe, GPi, SNr and ventral pallidum. Additionally, light cytoplasmic P90 immunolabeling was seen in WT SPNs.

We performed multiple immunofluorescence with NeuroTrace 435/455 as a counterstain on Q175 striatum to determine the neuron-type specific localization of 11G2+ immunolabeling, as imaged using CLSM. These studies showed that 11G2 immunolabeling at 10 months of age

in Q175 mice accumulates diffusely and as aggregates in the nuclei of the vast majority of striatal neurons, which by their abundance and size are likely to be SPNs (Fig. 1I-L). By this age, nuclear aggregates are, however, far more common and evident than the diffuse nuclear 11G2+ immunolabeling, which we saw prevailed at 2 months of age. The CLSM imaging also showed that a mix of small and larger 11G2+ aggregates was widespread in the neuropil of striatum at 10 months. Nuclear aggregates were typically larger than neuropil aggregates. Using interneuron markers, we observed that no cholinergic (ChAT+) interneurons possessed diffuse nuclear 11G2, 13.6% possessed cytoplasmic aggregates, and 2.3% possessed nuclear aggregates (Fig. 2A-C). By contrast, 11G2 signal was much more common in PARV+ striatal interneurons, with 48.1% possessing diffuse nuclear labeling, 36.5% possessing nuclear aggregates, and 9.6% possessing cytoplasmic aggregates (Fig. 2D-F). The nuclear aggregates were typically present in PARV+ interneurons also possessing diffuse nuclear P90, and nuclear aggregate size was less than in SPNs. In some cases, multiple tiny nuclear aggregates were present in PARV+ interneurons, seemingly a precursor to their coalescence into a larger aggregate. We additionally examined GPe using multiple immunofluorescence, and found that the PARV+ orthotypic neurons were devoid of diffuse nuclear 11G2+ immunolabeling, in contrast to PARV+ striatal interneurons, although about 5% possessed either nuclear or cytoplasmic aggregates (Fig. 2G-I). PARV-negative GPe neurons were also poor in 11G2 signal.

We scored the basal ganglia 11G2 immunolabeling on a 0-4 scale at 2-, 6-, 12- and 18-months of age, with 0 indicating no labeling and 4 indicating extremely pervasive labeling, as described in the Methods section. For any given region with perikaryal labeling, the labeling progressed from initially diffuse-only nuclear perikaryal localization to aggregate labeling in nuclei becoming common but not entirely superseding the diffuse nuclear labeling. Table 3

shows higher 11G2+ load for striatal structures (somatic striatum, accumbens, olfactory tubercle) than for pallidal (GPe, GPi, SNr, and ventral pallidum), which is consistent with the much higher vulnerability of striatum than pallidum in HD (Vonsattel, 2008; Reiner et al., 2011).

P90 Labeling of dSPNs versus iSPNs in Q175 Mouse. We used D1 immunolabeling to distinguish dSPNs (D1-rich) from iSPNs (D1-poor) (Lei e al., 2004; Deng et al., 2006), in conjunction with NeuN immunolabeling and NeuroTrace 435/455 staining to define the boundaries of neuronal nuclei and perikarya, and 11G2 immunolabeling. Surprisingly, we found that at 6 months of age, the presumptive dSPNs contained a 47.1% greater load of diffuse 11G2 by percent of cell area occupied than did the presumptive iSPNs, a difference that was significant for the 228 iSPNs and 228 dSPNs analyzed. There was, however, no significant difference between presumptive dSPNs and presumptive iSPNs in the 11G2+ areal aggregate load as a percent of cell area at 6 months. The aggregate area was, however, slightly greater (12.4%) in D1-rich presumptive dSPN perikarya. By contrast, at 18 months of age, when aggregates have become more prominent, the presumptive dSPNs and presumptive iSPNs did not differ significantly in their diffuse 11G2 load (Table 4). In the case of aggregated 11G2 signal, the load at 18 months in D1-poor (iSPN) perikarya exceeded that in D1-rich (dSPN) perikarya by 11.4% (Table 4), but this difference was not statistically significant. Thus, although a slightly higher 11G2 aggregate load may occur in presumptive iSPNs at this older age, at the younger age dSPNs show much greater enrichment in diffuse 11G2 signal.

P90 Labeling in Q175 Mouse Cerebral Cortex, Hippocampus, Amygdala and Diencephalon. Both the 11G2 and 1B12 antibodies detected huntingtin in 2-, 6-, 10-, 12-, and 18-month old Q175 mice (Figs. 1, 3). In cerebral cortex, we observed diffuse nuclear immunolabeling in layer 4 of somatosensory cortex at 2 months of age, as also reported by Smith

et al. (2023) using the S830 antibody, and by 6 months we saw widespread diffuse nuclear immunolabeling of neurons across cortical layers (Fig. 3B-D). The P90 immunolabeling, however, was less prevalent in layer 5 than the other layers, and less common in layer 5B than layer 5A. We performed multiple immunofluorescence with NeuroTrace 435/455 to determine the cellular localization of 11G2+ immunolabeling. We found that 11G2 immunolabeling at 6-12 months of age in Q175 mice accumulates in cortex largely as aggregates in the nuclei of cortical neurons in layers 2-4 and 6, but largely in the neuropil of layer 5 (Fig. 3E-H). Of note, we saw 11G2 and 1B12 cortical immunolabeling in WT mice (i.e., Q175 WT littermates) that resembled what we have seen with antibodies against WT huntingtin – namely immunolabeling of the cytoplasm of layer 5 cortical neurons (Fig. 3A) (Fusco et al., 1999; Dragatsis et al., 2018).

In the Q175 hippocampal complex, slightly above WT background levels of diffuse P90+ immunolabeling was seen in CA1 pyramidal neurons and dentate gyrus granule cells at 2 months, more so CA1, but neuropil labeling was absent. Immunolabeling in the majority of neurons in the thalamus and hypothalamus was largely at background levels at 2 months (Fig. 1B). Although light diffuse perikaryal labeling was evident in the paraventricular nucleus of the hypothalamus (PVN) of mutants (Fig. 4E), similar labeling was seen in 2-month old WT mice (Fig. 4A). By 6 months of age, hippocampal pyramidal neuron labeling in the cornu ammonis (CA) field had become much more prominent, with neurons of CA1, CA3 and CA4 but not CA2 highly enriched. The labeling was largely nuclear, with diffuse labeling and aggregates present in every CA1 neuron cell body, but only diffuse nuclear labeling evident in CA3 and CA4. Labeling of dentate gyrus granule cells was more prominent than at 2 months, consisting of intense diffuse nuclear labeling, and punctate labeling in the neuropil of the dentate hilus was also much more prominent. Immunolabeling in thalamus was advanced beyond that at 2 months,

with diffuse nuclear P90 signal evident in neurons of the posterior, lateral posterior, midline thalamic nuclei, and in the parafascicular nucleus (PFN). P90 labeling of hypothalamus in general remained sparse, but the diffuse cytoplasmic PVN labeling remained evident in WT mice (Fig. 4B), and in Q175 mice diffuse nuclear labeling of PVN neurons was now evident (Fig. 4F). By 12 months, intense diffuse nuclear labeling and intensely labeled nuclear aggregates were seen in all neurons of the dentate gyrus (granule cell layer and hilus both), CA1, CA3, and CA4 (Fig. 5). Labeling in CA2, by contrast, was mainly diffusely nuclear. The thalamus by 12 months showed widespread diffuse labeling of neuronal nuclei, again mainly in the posterior, lateral posterior, midline thalamic nuclei, and PFN (Fig. 1C). At this age, the PVN of hypothalamus was densely packed with neurons with diffuse nuclear P90 signal in mutants (Fig. 4G), while in WT PVN the P90 immunolabeling was as it was at 2 months (Fig. 4C). The overall regional labeling was similar at 18 months, but with nuclear aggregates larger where they were present at 12 months and now accompanied by neuropil aggregates as well, and regions showing mainly diffuse nuclear P90 now also showing nuclear aggregates (Fig. 1D). Hypothalamus was poor in P90 signal, in keeping with its low huntingtin expression, with PVN being an exception, as its neurons possessed diffuse nuclear P90 in mutants (Fig. 4H). Thalamic labeling was pervasive, with all thalamic cell groups now showing at least intense diffuse nuclear labeling (Fig. 1D), and PFN among the more enriched, in keeping with its high huntingtin expression (Allen Mouse Brain Atlas, 2004). Notable from 6 months on was the intense labeling of pyriform cortex neurons, beginning as mainly diffuse nuclear at 6 months and progressing to the presence of large aggregates in all pyriform cortex neurons, as well as in neuropil (Fig. 1C, D). We scored the 11G2 immunolabeling on a 0-4 scale at 2-, 6-, 12- and 18-months of age (Table 3). In multiple immunofluorescence with NeuroTrace 435/455 counterstain, we observed

that both 11G2+ aggregates and diffuse labeling were sparse in PARV+ cortical interneurons (Fig. 6). Finally, we found that the 11G2+ neuropil aggregates that predominate in layer 5 of cortex at 10-12 months of age did not align with SMI32+ processes in cortex (Fig. 7).

Specificity of P90 Antibodies in Mice. We immunolabeled sections from N171-Q82 mice with the P90 antibodies at 4 months of age, when they are known to form mutant protein aggregates (Schilling et al., 1999). Since N171-Q82 mice do not produce the mutant exon 1 huntingtin fragment, the N171-Q82 mice serve as negative controls for the specificity of the antibodies for the P90 neo-epitope. Our immunolabeling confirmed that there was no diffuse nuclear or aggregated P90 signal in N171-Q82 brain, while robust PHP1 immunolabeling of aggregates was observed in these same mice, representing detection of the aggregated N171 mutant protein (Fig. 8). This result suggests that the diffuse nuclear immunolabeling, and the nuclear and neuropil aggregate immunolabeling observed with the P90 antibodies in Q175 mice represents detection of the mutant human exon 1 protein, but not mutant huntingtin forms with amino acids beyond the exon 1 sequence. We saw similar results with the MW8 antibody, confirming the findings of Smith et al. (2023), indicating that MW8 too does not detect a form of the huntingtin protein that extends beyond exon 1.

To determine if the P90 antibodies are actually detecting more than exon 1 huntingtin, despite the biochemical evidence for their exon 1 protein selectivity (Missineo et al., 2024), we examined tissue from mice with tamoxifen-driven huntingtin deletion, and control conditional mice without deletion (Bragg et al., 2024). In mice with a 90% huntingtin deletion, as demonstrated in prior studies (Bragg et al., 2024) and our own immunolabeling with the D7F7 antibody against full-length huntingtin, we saw substantially diminished 11G2 immunolabeling of layer 5 cortical neurons, striatal neurons, and SPN terminals in striatal target areas, with the

remaining 11G2 signal presumably due to the residual neurons without huntingtin deletion (Fig. 9). This result favors the interpretation that 11G2 in WT mouse detects some level of production of exon 1 protein from WT huntingtin.

P90 Signal Overlap with MW8 and PHP1 in Q175 Mice. To gain insight into the relationship of P90 signal to the mutant huntingtin signal with other antibodies, we used multiple immunofluorescence to compare 11G2, MW8 and PHP1 in 6-month old, 12-month old, and 18-month old Q175 mice. We found that at six months the MW8+ signal occupies only the center of 11G2+ aggregates in striatum, and diffuse nuclear labeling was present but not as salient as for 11G2 (Figure 10). The aggregate area occupied by PHP1 signal at six months was even less, and diffuse nuclear labeling was again less salient than for 11G2. By 12 months, both MW8 signal and PHP1 signal occupied more of the central 11G2+ area of each aggregate, but still not its entirety (Fig. 10). Diffuse nuclear labeling was much reduced for 11G2 but still present, but again much less salient for MW8 and PHP1. These trends continued out to 18 months, with MW8 and PHP1 signal filling more of the 11G2+ area of each aggregate, but never its entirety. Similar results were obtained for cerebral cortex at 12 and 18 months for the three antibodies, when aggregate immunolabeling for MW8 and PHP1 first becomes noteworthy. As for striatum, the MW8+ and PHP1+ area of any given aggregate was less than for 11G2 and occupied the center of the 11G2+ aggregate (Fig. 11).

P90 Labeling in Human Basal Ganglia. We found that both the 11G2 and 1B12 antibodies detected aggregates in HD human basal ganglia and cortex. Control brain did not label for these, PHP1 or MW8. Because the 11G2 yielded more robust labeling than the 1B12, we used immunofluorescence with it in combination with NeuroTrace to assess the localization of 11G2 in caudate and putamen. The 11G2 immunolabeling was mainly observed in neuropil

aggregates in grade 1 through grade 4 HD striatum, with 11G2+ aggregates less common at grade 4 (Fig. 12). Nucleus accumbens was slightly richer than caudate and putamen. In our DAB-labeled tissue, we observed 11G2+ aggregates in the neuropil of GPe, GPi, SNr, and VP, but fewer than in striatum. The regional 11G2 localization scores for basal ganglia are shown in Table 5. We also assessed 11G2 immunolabeling in caudate and putamen in combination with immunofluorescence for PHP1 and MW8 (Fig. 13). 11G2 tended to detect many but not all of the same aggregates as PHP1. Moreover, for any given aggregate detected by both, the aggregate area was less with 11G2 and more centrally located. In the case of MW8, the overlap with 11G2 was more complete, which is not surprising since both are directed at the C-terminus of exon 1, while PHP1 is directed at its proline-rich domain. MW8+ aggregates that were 11G2-negative were seen, however. Aggregates that only labeled with 11G2 were rare.

P90 Antibody Studies in Human Cortex. We found that both the 11G2 and 1B12 antibodies detect aggregated exon 1 huntingtin protein in HD human cortex. As for basal ganglia, we examined 11G2 localization in comparison to PHP1 and MW8 localization, in this instance in A9 cortex in grade 1 and grade 4 cases (Figs. 14, 15). Aggregates at both grades were located mainly in the neuropil and most concentrated in layer 5. MW8 and 11G2 generally detected the same aggregates, which were a subset of those detected by PHP1. When detecting the same aggregates, MW8 and 11G2 labeled the center of the PHP1+ area. We assessed if the neuropil 11G2+ aggregates that predominate in HD cortex are localized to dendrites. To this end, we triple labeled tissue for 11G2, SMI32 and NeuroTrace (Fig. 16). We found that many large 11G2+ aggregates were encapsulated within SMI32+ processes in cortex. Additionally, some smaller 11G2+ aggregates aligned with what appeared likely to be dendritic spines. These

observations are consistent with Gutekunst et al. (1999). The regional 11G2 localization scores for pallial and diencephalic structures are shown in Table 5.

Discussion

In the present study, we show that the mutant huntingtin exon 1 protein does accumulate and aggregate in both Q175 mouse brain and human HD brain, as expected from the work of others (Sathasivam et al., 2013; Neueder et al., 2017; Smith et al., 2023). Moreover, the magnitude of the differential regional accumulation of exon 1 protein in forebrain is many regards consistent with the differential vulnerability of those regions in HD. Nonetheless, accumulation for some regions and some neuron types was inconsistent with a determinative role of mutant protein abundance in the vulnerability differences for those regions and those neuron types. Moreover, the differences between mutant mice and HD humans in the role of somatic expansion of the CAG repeat in the disease process need to be taken into account in comparing the current Q175 mouse and human HD results, as discussed in more detail below.

Exon 1 Protein Accumulation – HD mice and humans. In Q175 mice but not N171-82Q mice, the P90 antibodies yielded immunolabeling in many neurons throughout brain, showing that neurons in Q175 mice but not N171-82Q mice produce the mutant exon 1 protein. This supports the selectivity of the P90 antibodies for the exon 1 protein, as the chimeric mutant huntingtin gene in Q175 mice produces exon 1 protein due to the same splicing anomaly that occurs in human HD cases (Sathasivam et al., 2013; Neueder et al., 2017). By contrast, the transgene in N171-82Q mice spans exons 1 and 2, and is thus not subject to the same splicing anomaly that leads to mutant exon 1 protein build-up in Q175 mice and human HD (Schilling et al., 1999; Smith et al., 2023). Although the P90 antibodies do not distinguish between mutant

and WT human exon 1, as their epitope is the eight C-terminal residues of exon 1 shared in mouse and human, they potently detect mutant exon 1 because of its propensity to oligomerize and accumulate as aggregates. Nonetheless, we did see P90 immunolabeling in WT mice in some neuronal populations that also immunolabel with antibodies against full-length huntingtin (Fusco et al., 1999; Dragatsis et al., 2018). This immunolabeling was reduced in mice with 90% reduction in WT huntingtin, suggesting that WT mice do produce some amount of exon 1 protein in some neuronal populations from their endogeneous WT huntingtin alleles, in general proportion to the production of WT huntingtin in those populations. Consistent with our interpretation, Sapp et al. (2025) report low levels of the exon 1 protein in control human brain.

P90 signal was largely localized to SPNs at 2 months of age in Q175 heterozygotes, manifesting as diffuse nuclear labeling. A similar result was reported by Smith et al., (2023) using the S830 antibody against mutant exon 1. The early preferential accumulation of exon 1 protein in the nuclei of SPNs indicates that even when all neurons in the brain possess a huntingtin gene with the same expanded pathogenic repeat, SPNs are still nonetheless prone to accumulating more of this protein – consistent with their greater vulnerability in HD. The early occurrence at 2 months of diffuse nuclear localization of mutant exon 1 in SPNs is associated with a slight reduction in preproenkephalin expression by iSPNs (Deng et al., 2021). With age progression, mutant exon 1 accumulation gradually becomes yet more prominent in striatum, and more widespread in the brain, with nuclear aggregates and/or neuropil aggregates present in many brain regions, and neurochemical and behavioral deficits more evident (Deng et al., 2021).

We probed the composition of the aggregates, comparing labeling with 11G2 with labeling obtained using the PHP1 and MW8 antibodies in striatum and cortex of 6-18 month old Q175 mice. At six months, the MW8+ signal occupied only the center of 11G2+ aggregates in

Q175 striatum. The aggregate area occupied by PHP1 signal at six months was even less. By 12 months, both MW8 signal and PHP1 signal occupied more of the 11G2+ aggregate area, but still not its entirety. Thus, our results show that the PHP1 and MW8 target epitopes are only antibody-accessible in the core of the 11G2+ aggregates in these mice, and that the epitope targeted by MW8 is very similar but not the same as that for 11G2, as also reported by Sapp et al. (2025). Additionally, at both ages, diffuse nuclear signal was more evident with 11G2 than PHP1 and MW8, indicating that the C-terminus of the exon 1 protein is more accessible to the P90 antibodies in its diffuse, presumably monomeric or oligomeric, form in Q175 mice, than the polyproline region of the exon 1 protein detected by PHP1. Our results thus show that the presumably toxic huntingtin mutant exon 1 protein is more pervasive in Q175 mouse than revealed by antibodies such as PHP1 and MW8.

In our human HD cases as well, the P90 antibodies yielded clear immunolabeling of aggregates, albeit with far less regional density than in Q175 mouse. As the exon 1 huntingtin protein has been shown to be produced in human HD brain (Sathasivam et al., 2013; Neueder et al., 2017; Sapp et al., 2025), our human findings with the P90 antibodies show that the exon 1 protein accumulates and forms aggregates in HD brain. Although P90+ nuclear and neuropil aggregates were both common in Q175 mice, especially older ones, the P90 antibodies in human HD cases mainly labeled neuropil aggregates in striatum and cortex. Similarly, prior studies using other antibodies have also found mutant protein aggregates in only a small percent of human striatal neurons of HD patients (DiFiglia et al., 1997; Maat-Schieman et al., 1999; Gutekunst et al., 1999; Kuemmerle et al., 1999), despite their prominence in striatal neurons in mouse models of HD (Meade et al., 2002; Brooks and Dunnett, 2015). Part of the explanation for this difference for striatum at least may stem from the asynchronous nature of the CAG

repeat expansion required for mutant protein production and accumulation in the human disease (Mätlik et al., 2024; Handsaker et al., 2024). It seems likely that, at any moment in time, only a small number of SPNs will have progressed to a repeat expansion sufficient to yield exon 1 protein accumulation, and that neurons die relatively rapidly after reaching this point. Extrapolating from Q175 mice, which show no SPN death at 18 months even (Deng et al., 2021), SPNs in human HD would be expected to survive at least 18-24 months upon reaching 190 repeats. Although this consideration may explain why aggregates per se are scarce in human striatum, it does not explain why neuropil aggregates predominate. As SPN vulnerability to mutant protein in mouse models seems to involve a pathogenic effect in the nucleus (Benn et al., 2005; Dragatsis et al., 2009; Gu et al., 2015), the predominantly non-nuclear localization in human HD striatum raises questions about the pathogenic mechanism of mutant huntingtin in SPNs. It is possible that the suboptimal fixation of human tissue obscures some of the mutant exon 1 localization. Aggregates immunolabeled for 11G2 were somewhat more common in cerebral cortex in HD brain than in striatum, but in cortex as well they were largely restricted to the neuropil, in many cases to dendrites. This raises questions about the mechanism by which mutant exon 1 accumulation injures cortical neurons. Nuclear accumulation clearly can disrupt transcriptional activity, but dendritic or axonal localization could also adversely and deleteriously impair cell function and viability (Gutekunst et al., 1999).

Differential Regional and Cellular Vulnerability – HD mice and humans. For both Q175 mice and human HD brains, the overall regional distribution of 11G2+ signal in forebrain, as well as specifically in basal ganglia structures, appeared consistent with the HD vulnerability of those regions. For example, 11G2 content was higher in more vulnerable basal ganglia structures than less vulnerable pallial structures, and greater in the more vulnerable striatal than

the less vulnerable pallidal structures. In relating mouse to human, however, it needs to be noted that a key factor in mutant huntingtin exon 1 accumulation in humans is the regional differences in somatic expansion of the CAG repeat (Mätlik et al., 2024; Pressl et al., 2024; Handsaker et al., 2025). This phenomenon seems, in particular, to explain the greater vulnerability of SPNs than other cell types in HD (Mätlik et al., 2024; Pressl et al., 2024; Handsaker et al., 2025). The greater vulnerability of iSPNs relative to dSPNs, despite the inherently greater propensity for mutant protein accumulation we saw in dSPNs relative to iSPNs in Q175 mice, is perhaps explainable by a slightly greater propensity of iSPNs for CAG expansion (Handsaker et al., 2025). Without expansion to the 150 repeats suggested by Handsaker et al. (2025) as needed for pathogenesis, cell types that produce copious exon 1 protein in Q175 mouse, might make much less in human HD brain. This may explain why structures such as CA1 and pyriform cortex, which show an extreme accumulation of exon 1 protein in all neuronal nuclei in Q175 mice, have not been found to show notable pathology in HD (Spargo et al., 1993; Reiner et al., 2011).

On the other hand, some neuron types, such as striatal cholinergic interneurons, are known to show somatic expansion in human HD (Mätlik et al., 2024; Handsaker et al., 2025) and produce large amounts of huntingtin (Fusco et al., 1999), but nonetheless were found by us to show little exon 1 protein aggregate formation. The meager accumulation of mutant exon 1 protein in cholinergic interneurons in Q175 mice, while consistent with their resistance in HD (Massouh et al., 2008), is not predictable from their expected large production of mutant exon 1 protein. Possibly, cholinergic interneurons may have more active degradative mechanisms (Waelter et al., 2001; Zhao et al., 2024). On the other hand, PARV+ striatal interneurons show little somatic expansion in human HD (Mätlik et al., 2024; Handsaker et al., 2025), yet their HD vulnerability is comparable to that of iSPNs (Reiner et al., 2013). Our results for Q175 mice

show that with a CAG repeat length of 190, PARV+ interneurons accumulate more mutant exon 1 protein than do cholinergic interneurons. With their limited somatic expansion in human HD, however, PARV+ interneurons would not be expected to accumulate pathogenic levels of mutant exon 1, raising questions then about the basis of their loss in human HD.

The vulnerability of layer 5A cortical neurons in HD (Reiner et al., 2011) relative to their low levels of exon 1 protein accumulation is of interest as well. Neurons of cortical layer 5A project only within telencephalon, inclusive of other cortical areas and striatum, and are thus termed intratelencephalically projecting cortical neurons (IT-type) (Reiner et al., 2003). The neurons of layer 5B also project to striatum, but to brainstem and spinal cord as well via the pyramidal tract, and are thus called pyramidal-tract type (PT-type) (Reiner et al., 2003). The IT neuron type or a subset of it has been found to show somatic expansion in human HD, while the PT-type or a subset of it does not (Pressl et al., 2024). Although neuropathological studies have not reported differential pathology of layer 5A versus 5B neurons in HD (Reiner et al., 2011), Pressl et al. (2024) report greater loss of 5A than 5B neurons in HD, and similarly Deng et al. (2014) report greater loss of IT-type corticostriatal terminals (i.e., 5A) than PT-type corticostriatal (i.e., 5B) terminals in Q140 mouse. Surprisingly, we observed lesser exon 1 protein accumulation in layer 5A neurons than 5B neurons in Q175 mice. Layer 5A and 5B neurons are, however, not just singular types and each possesses a diversity of subtypes (Sorensen et al., 2015; Bakken et al., 2021; Hausmann et al., 2022). It would be useful to relate that diversity to somatic expansion in human HD, their vulnerability in HD, and mutant protein accumulation in mouse HD models and in human HD.

Aggregate Composition. The relative localization of the epitopes detected by the 11G2, MW8 and PHP1 antibodies differed between Q175 mouse and human HD. In mouse, MW8 and

PHP1 signal occupied the core of aggregates defined by 11G2 signal, and showed less diffuse nuclear signal. Since all three antibodies target the exon 1 protein, the results suggest that in the oligomerization and aggregation process, the 11G2 epitope remains accessible throughout, while the MW8 and PHP1 epitopes are cryptic or largely so, during the oligomer stage and parts of the aggregation stage in mouse. By contrast, in human HD, MW8 and 11G2 generally detected the same aggregates, which were a subset of those detected by PHP1. When detecting the same aggregates as PHP1, the MW8 and 11G2 antibodies labeled the center of the PHP1+ area. These results seem to suggest that the aggregated mutant exon 1 targeted by MW8 and 11G2 might be the seeds around which the aggregate enlarges in HD brain, with the aggregate periphery potentially including larger forms of the mutant protein and WT protein (Sapp et al., 2025). The interpretation of these results needs to take into consideration the suboptimal fixation of human tissue compared to Q175 tissues, and the antigen retrieval used in human but not mouse – both of which affect antigen accessibility (Meade et al., 2002; Bayram-Weston and Weston, 2016; Smith et al., 2023). Nonetheless, we know from our own studies that antigen retrieval does not affect PHP1 and MW8 localization in Q175 mouse, and so it seems unlikely that antigen retrieval alone accounts for the human – mouse difference we see in the relative localization of 11G2, MW8 and PHP1 signal. Whether fixation conditions accounts for the mouse – human difference in aggregate epitope localization, and which in any case provides the truer insight into aggregate composition and formation in human disease, is uncertain.

Acknowledgements

We thank Dr. Jeff Carroll of the University of Washington, Dr. Deanna Marchionini of the CHDI, and Dr. Wenzhen Duan of Johns Hopkins University for providing tissues used in this study. We thank the CHDI for providing the P90 antibodies, and Drs. Liliana Menalled, Liz Doherty, and Jonathan Bard for details about antibody production and comments on this manuscript. This study was supported by the CHDIF (AR).

Author contributions
YD, MJ and RC conducted the studies. YD and AR conducted analysis. AR, YD and MJ prepared the manuscript.

Ethical considerations
All animal use was carried out in accordance with the National Institutes of Health Guide for Care and Use of Laboratory Animals and Society for Neuroscience Guidelines, and with the approval of the University of Tennessee Health Science Center Animal Care and Use Committee (approval # 21-0308) on November 8, 2021. All human studies were conducted on de-identified postmortem tissue, and thus the University of Tennessee Health Science Center Institutional Review Board waived the requirement for approval (16-04430-NHSR), and no informed consent was required.

Consent to participate
Not applicable.

Consent for publication
Not applicable.

Declaration of conflicting interest
The authors declare no conflicts of interest with respect to the research, authorship, and/or publication of this article.

Funding statement
The authors disclose receipt of the following financial support for the research, authorship, and/or publication of this article: This work was supported by the Cure Huntington's Disease Initiative (grant number A-17067).

Data availability
Data collected as part of this study will be made available upon reasonable request.

Figure Legends

Figure 1. The first two rows of images showing P90 immunolabeling with the 11G2 antibody in 2-month old (B, F), 10-month old (C, G), and 18-month old Q175 (D, H) mice compared to a 10-month old WT littermate control (A, E), with the first row showing an entire section through the right side of the forebrain at the level of GPe, and the second row showing a view of right dorsolateral striatum. 11G2 immunolabeling of perikarya in the Q175 mice at 2 months is diffuse and appears to be nuclear, with nuclear and neuropil aggregates forming with age progression, and lessened diffuse nuclear labeling. Images I and K show a merged CLSM image of striatum from a 6-month old Q175 mouse and a 12-month old Q175 mouse, respectively, with striatal neurons labeled blue with NeuroTrace (NT) and 11G2 immunolabeling in green. Images J and L show the 11G2 immunolabeling alone for these cases. The CLSM images show diffuse and aggregated 11G2 signal in striatal neurons at 6 months, with nuclear and neuropil aggregates more prominent at 12 months. Note, however, that image A shows that 11G2 immunolabeling is present in terminals in GPe in WT mice, suggesting 11G2 detects exon 1 protein derived from WT mouse huntingtin as well. The higher power view in image E of WT striatum shows that light cytoplasmic 11G2 immunolabeling is present in numerous presumptive striatal projections neurons in WT mouse (some indicated by small asterisks). Scale bar in B applies to all images in first row, scale bar in E applies to all images in second row, scale bar in I applies to both images in third row and scale bar in K applies to both images in last row.

Figure 2. The first image in each of the first two rows shows a merged CLSM image of striatum from a 10-month old Q175 mouse with striatal neurons labeled blue with NeuroTrace, 11G2+ aggregates shown in green, and the interneuron marker (ChAT in the upper row, PARV in the lower row) shown in red. The second image in each row shows the green channel and blue channel only from the merged images, and the last image in each row shows the 11G2 green channel from the merged image. The arrows in each row indicate the interneurons. Note the ChAT interneurons are largely devoid of 11G2 but the PARV interneurons commonly show diffuse and aggregated 11G2 signal in their nuclei. The last row shows a merged CLSM image of GPe from a 10-month old Q175 mouse with GPe neurons labeled blue with NeuroTrace, 11G2+ aggregates shown in green, and PARV+ orthotypic GPe neurons shown in red (some indicated by arrows). The second image in this row shows the green channel and blue channel only from the merged image, and the last image shows the 11G2 green channel from the merged image. While small 11G2+ aggregates are common in the GPe neuropil, 11G2 signal is sparse in both PARV+ orthotypic GPe neurons and presumptive arkypallidal PARV-negative GPe neurons. Scale bar in A applies to all images in first two rows, and scale bar in G applies to all images in last row.

Figure 3. The first row of images shows P90 immunolabeling with the 11G2 antibody in 2-month old (B), 10-month old (C), and 18-month old Q175 (D) mice compared to a 10-month old WT littermate control (A) throughout the depth of somatosensory cortex, using DAB labeling. 11G2 immunolabeling of perikarya in the Q175 mice at 2 months manifests mainly as diffuse nuclear labeling of layer 4 neurons. Subsequently, diffusely nuclear labeling appears in neurons of most layers followed by nuclear and neuropil aggregate formation. Images E and G show a merged CLSM image through the depth of somatosensory cortex from a 6-month old Q175 mouse and a 12-month old Q175 mouse, respectively, with striatal neurons labeled blue with

NeuroTrace (NT) and 11G2 immunolabeling in green. Images F and H show the 11G2 immunolabeling alone for these cases. The CLSM images show diffuse and aggregated 11G2 signal in some cortical neurons at 6 months, with nuclear and neuropil aggregates more prominent at 12 months. Note, however, that image A shows that 11G2 immunolabeling is present in the cytoplasm of many layer 5 neurons in WT mice, suggesting 11G2 detects exon 1 protein derived from WT mouse huntingtin. Scale bar in B applies to images in first row, and scale bar in F to images in second row.

Figure 4. The first row of images shows P90 immunolabeling in the right paraventricular nucleus of the hypothalamus (PVN) with the 11G2 antibody in 2-month old (A), 6-month old (B), 12-month old Q175 (C), and 18-month old WT (D) mice, while the second row shows the PVN immunolabeling for 11G2 in 2-month old (E), 6-month old (F), 12-month old (G), and 18-month old Q175 (H) mice. Diffuse cytoplasmic immunolabeling and some neuropil immunolabeling makes the PVN stand out from the surrounding hypothalamus in WT mice. Similar immunolabeling occurs in 2-month Q175 mice (E), but by 6 months and thereafter PVN neurons show distinct diffuse nuclear 11G2 (F-G). Scale bar in A applies to all images.

Figure 5. Images showing P90 immunolabeling with the 11G2 antibody in the right-side hippocampus of 12-month old Q175 mouse. Image A shows hippocampus with neurons labeled blue with NeuroTrace (NT) and 11G2 immunolabeling in green. Images B, C, and D show merged CLSM images of CA1, CA2/CA3, and dentate gyrus, respectively, with neurons labeled blue with NT and green for 11G2. Images E, F and G show the 11G2 immunolabeling alone for these same fields, respectively. The CLSM images show diffuse and aggregated nuclear 11G2 signal in CA1, CA3 and dentate granule cell layer neurons, but mainly diffuse nuclear signal in CA2. Scale bar in B apples also to E, scale bar in C applies also to F, and scale bar in D applies also to G.

Figure 6. The first row shows a single CLSM field of view of somatosensory cortex from a 10-month old Q175 mouse with cortical neurons labeled blue with NeuroTrace (NT), 11G2+ aggregates shown in green, and PARV+ interneurons shown in red, with the panels A-C each showing the labeling in different combinations, and D and E showing the 11G2 and NT signal alone, respectively. The second and third rows shows higher power images of parts of the same field of view as in the first row. The first column shows the 11G2, PARV, and NT signals for layer 3 (F) and layer 5 (I), respectively, with arrows in each row indicating some of the interneurons. The subsequent columns show the 11G2 and NT signals (G, J), and the 11G2-only signal (H, K), with arrows indicating the same interneurons as in the first column. In general, 11G2+ signal is sparse in PARV+ cortical interneurons. Scale bar in C applies to images in first row, scale bar in H applies to images in second row, and scale bar in K applies to images in third row.

Figure 7. Images showing a merged CLSM image of layer 5 (L5) of somatosensory cortex from a 12-month old Q175 mouse with cortical neurons labeled blue with NeuroTrace (NT), 11G2+ aggregates shown in green, and the pyramidal neuron dendrite marker SMI32 shown in red. Although 11G2+ aggregates not localized to neuronal nuclei are present (i.e., neuropil aggregates), none are localized to the SMI32+ dendrites. Thus, neuropil aggregates appear to be

localized to terminals or SMI32-negative dendrites in Q175 cortex. Scale bar in B applies to both images.

Figure 8. Images comparing P90 11G2 immunolabeling and PHP1 immunolabeling in cortex and striatum of a 4-month old N171-82Q mouse. No specific 11G2 immunolabeling is present in the cortex, striatum (A, C), or any other brain area in the N171-82Q mouse. By contrast, widespread cortical and striatal immunolabeling was seen with PHP1 (B, D). Scale bar in A applies to all images.

Figure 9. Immunolabeling in striatum at the level of GPe for D7F7 (A, B) and 11G2 (C, D) in huntingtin-flox mice with a tamoxifen inducible Cre recombinase, i.e. Httflox/flox;CAG-CreERT (Bragg et al., 2024), without tamoxifen treatment (A, C) and with tamoxifen treatment (B, D). The mice were 3 months old and one month post vehicle or tamoxifen treatment. In the mice without tamoxifen treatment, and thus with normal levels of WT huntingtin, both the D7F7 antibody against full-length huntingtin (A) and 11G2 (C) yielded immunolabeling of terminals in GPe, presumably of SPN origin. In the tamoxifen-treated mouse, the D7F7 immunolabeling of GPe fibers was substantially reduced but not entirely eliminated, consistent with prior evidence that WT huntingtin levels are 90% reduced by tamoxifen treatment (Bragg et al., 2024). In the same mouse, 11G2 immunolabeling of GPe fibers was also substantially reduced but not completely eliminated (D), suggesting that 11G2 in WT mouse detects some level of production of exon 1 protein from WT huntingtin. Scale bar in B applies to all images. Abbreviation: internal capsule – IC.

Figure 10. The first two rows show a CLSM image of a single field of view of striatum from a 6-month Q175 mouse from tissue that had been simultaneously immunolabeled for 11G2, MW8 and PHP1, while the last two rows show a CLSM image of a single field of view of striatum from a 12-month Q175 mouse from tissue that had been simultaneously immunolabeled for 11G2, MW8 and PHP1. The first and third row show in succession the merged CLSM image for 11G2 (green), MW8 (red) and NeuroTrace (blue) in the first column, the merged 11G2 and MW8 image in the second column, and the MW8-only image in the third column. The second and fourth row show in succession the merged CLSM image for 11G2 (green), PHP1 (red) and NeuroTrace (blue) in the first column, the merged 11G2 and PHP1 image in the second column, and the PHP1-only image in the third column. Note that at 6 months the MW8+ signal occupies only the center of 11G2+ aggregates, and diffuse nuclear labeling is not prominent for MW8. The aggregate area occupied by PHP1 signal at six months is slightly greater, but diffuse nuclear labeling is again meager. By 12 months, both the MW8 signal and the PHP1 signal occupy more of the 11G2+ area of each aggregate, but still not its entirety. Scale bar in F applies to all images.

Figure 11. The first two rows show a CLSM image of a single field of view of layers 2 and 3 of somatosensory cortex from a 12-month Q175 mouse from tissue that had been simultaneously immunolabeled for 11G2, MW8 and PHP1, while the last two rows show a CLSM image of a single field of view of striatum from an 18-month Q175 mouse from tissue that had been simultaneously immunolabeled for 11G2, MW8 and PHP1. The first and third row show in succession the merged CLSM image for 11G2 (green), MW8 (red) and NeuroTrace (blue) in the first column, the merged 11G2 and MW8 image in the second column, and the MW8-only image

in the third column. The second and fourth row show in succession the merged CLSM image for 11G2 (green), PHP1 (red) and NeuroTrace (blue) in the first column, the merged 11G2 and PHP1 image in the second column, and the PHP1-only image in the third column. Note that at 12 months the MW8+ signal occupies only the center of 11G2+ aggregates, and diffuse nuclear labeling is not prominent for MW8. The aggregate area occupied by PHP1 signal at 12 months is slightly greater, but diffuse nuclear labeling is again meager. By 18 months, both MW8 signal and PHP1 signal occupy more of the 11G2+ area of each aggregate, but still not its entirety. Scale bar in F applies to all images.

Figure 12. CLSM images of a single field of view through caudate and putamen, respectively, from a grade 1 HD case (A, B) and a grade 4 HD case (C, D) immunolabeled green for 11G2 with NeuroTrace (blue). 11G2+ aggregates are sparse and localized to neuropil mainly. Scale bar in D applies to all images.

Figure 13. Each row presents a single CLSM field of view through caudate or putamen from a grade 1 HD case (A-E caudate, K-O putamen) or a grade 4 HD case (F-J caudate, P-T putamen) showing the green immunolabeling for 11G2 (first, second and last columns), and red for either MW8 (first and third column) or PHP1 (second and fourth column). Arrows indicate the 11G2+ aggregates in the field of view, which also tend to possess MW8 or PHP1 signal. PHP1 detects the largest aggregate area, while the more centrally located 11G2 and MW8 signals in each PHP1+ aggregate tend to be similar in areal extent. Scale bar in A applies to all images.

Figure 14. Immunofluorescence triple-label comparing localization of 11G2 (E) to that of MW8 (D) and PHP1 (C) in a single slab of A9 cortex of a grade 1 HD case. The first panel (A) shows the merged image for PHP1 and 11G2 with a NeuroTrace counterstain, and the second (B) shows a merged image for MW8 and 11G2 with a NeuroTrace counterstain. The last panel (F) shows NeuroTrace counterstain alone. The three antibodies largely detect the same aggregates, with PHP1 detecting more aggregates and more of any given aggregate area. Scale bar in C applies to all images.

Figure 15. Immunofluorescence triple-label comparing localization of 11G2 (E) to that of MW8 (D) and PHP1 (C) in single fields of view of layer 3 (row 1) and layer 5 (row 2) of A9 cortex from a grade 1 HD case. The first column (A, F) shows the merged image for PHP1 and 11G2 with a NeuroTrace counterstain, and the second (B, G) shows a merged image for MW8 and 11G2 with a NeuroTrace counterstain. The remaining three columns show the individual PHP1, MW8, and 11G2 signals, respectively. The three antibodies largely detect the same aggregates, with PHP1 detecting more aggregates and more of any given aggregate. Scale bar in A applies to all images.

Figure 16. Panels showing merged CLSM images of layer 5 of A9 cortex from a grade 1 HD case (A, B), a grade 2 case (C, D) and a grade 4 case (E, F), with cortical neurons labeled blue with NeuroTrace, 11G2+ aggregates shown in green, and the pyramidal neuron dendrite marker SMI32 shown in red. Many large 11G2+ aggregates are encapsulated by SMI32+ processes. Scale bar in E applies to all images.

Tables

Table 1. Antibodies used in present study.

Table 2. Human cases used in present study.

Table 3. Age-wise 11G2 scores for Q175 mouse for forebrain structures.

Table 4. 11G2 mutant exon 1 protein load for dSPNs versus iSPNs at 6 and 18 months of age in Q175 mice.

Table 5. Grade-wise 11G2 scores for human HD cases for forebrain structures.

References

Albin RL, Reiner A, Anderson KD, Penney JB, Young AB. Striatal and nigral neuron subpopulations in rigid Huntington's disease: implications for the functional anatomy of chorea and rigidity-akinesia. *Ann Neurol* 1990; 27: 357-365.

Allen Mouse Brain Atlas. *Allen Institute for Brain Science* 2004; Available from: http://mouse.brain-map.org.

Bakken TE, Jorstad NL, Hu Q, Lake BB, Tian W, Kalmbach BE, Crow M, Hodge RD, Krienen FM, Sorensen SA, Eggermont J, Yao Z, Aevermann BD, Aldridge AI, Bartlett A, Bertagnolli D, Casper T, Castanon RG, Crichton K, Daigle TL, Dalley R, Dee N, Dembrow N, Diep D, Ding SL, Dong W, Fang R, Fischer S, Goldman M, Goldy J, Graybuck LT, Herb BR, Hou X, Kancherla J, Kroll M, Lathia K, van Lew B, Li YE, Liu CS, Liu H, Lucero JD, Mahurkar A, McMillen D, Miller JA, Moussa M, Nery JR, Nicovich PR, Niu SY, Orvis J, Osteen JK, Owen S, Palmer CR, Pham T, Plongthongkum N, Poirion O, Reed NM, Rimorin C, Rivkin A, Romanow WJ, Sedeño-Cortés AE, Siletti K, Somasundaram S, Sulc J, Tieu M, Torkelson A, Tung H, Wang X, Xie F, Yanny AM, Zhang R, Ament SA, Behrens MM, Bravo HC, Chun J, Dobin A, Gillis J, Hertzano R, Hof PR, Höllt T, Horwitz GD, Keene CD, Kharchenko PV, Ko AL, Lelieveldt BP, Luo C, Mukamel EA, Pinto-Duarte A, Preissl S, Regev A, Ren B, Scheuermann RH, Smith K, Spain WJ, White OR, Koch C, Hawrylycz M, Tasic B, Macosko EZ, McCarroll SA, Ting JT, Zeng H, Zhang K, Feng G, Ecker JR, Linnarsson S, Lein ES. Comparative cellular analysis of motor cortex in human, marmoset and mouse. *Nature* 2021; 598: 111-119.

Bayram-Weston Z, Jones L, Dunnett SB, Brooks SP. 2016. Comparison of mHTT antibodies in Huntington's Disease mouse models reveal specific binding profiles and steady-state ubiquitin levels with disease development. *PLoS One* 11: e0155834.

Benn CL, Landles C, Li H, Strand AD, Woodman B, Sathasivam K, Li SH, Ghazi-Noori S, Hockly E, Faruque SM, Cha JH, Sharpe PT, Olson JM, Li XJ, Bates GP. Contribution of nuclear and extranuclear polyQ to neurological phenotypes in mouse models of Huntington's disease. *Human Mol Genetics* 2005; 14: 3065-3078.

Bragg RM, Mathews EW, Grindeland A, Cantle JP, Howland D, Vogt T, Carroll JB. Global huntingtin knockout in adult mice leads to fatal neurodegeneration that spares the pancreas. *Life Sci Alliance* 2024; 7: E202402571.

Brooks SP, Dunnett SB. Mouse models of Huntington's disease. *Curr Top Behav Neurosci* 2015; 22: 101-133.

Davies SW, Turmaine M, Cozens BA, DiFiglia M, Sharp AH, Ross CA, Scherzinger E, Wanker EE, Mangiarini L, Bates GP. Formation of neuronal intranuclear inclusions underlies the neurological dysfunction in mice transgenic for the HD mutation. *Cell* 1997; 90: 537-548.

Deng YP, Penney JB, Young AB, Albin RL, Anderson KD, Reiner A. Differential loss of striatal projection neurons in Huntington's disease: A quantitative immunohistochemical study. *J Chem Neuroanat* 2004; 27: 143-164.

Deng, YP, Lei WL, Reiner A. Differential perikaryal localization in rats of D1 and D2 dopamine receptors on striatal projection neuron types identified by retrograde labeling. *J Chem Neuroanat* 2006; 32: 101-116.

Deng YP, Wong T, Wan JY, Reiner A. Differential early loss of thalamostriatal and corticostriatal input to striatal projection neuron types in the Q140 Huntington's disease knock-in mouse model. *Front Systems Neurosci* 2014; 8: 198.

Deng Y, Wang H, Joni M, Sekhri R, Reiner A. Progression of basal ganglia pathology in heterozygous Q175 knock-in Huntington's disease mice. *J Comp Neurol* 2021; 529: 1327-1371.

DiFiglia M, Sapp E, Chase KO, Davies SW, Bates GP, Vonsattel JP, Aronin N. Aggregation of huntingtin in neuronal intranuclear inclusions and dystrophic neurites in brain. *Science* 1997; 277: 1990-1993.

Dragatsis I, Goldowitz D, Del Mar N, Deng YP, Meade CA, Liu L, Sun Z, Dietrich P, Yue J, Reiner A. CAG repeat lengths ≥335 attenuate the phenotype in the R6/2 Huntington's diseas transgenic mouse. *Neurobiol Dis* 2009; 33: 315-330.

Dragatsis I, Dietrich P, Ren H, Deng YP, Del Mar N, Wang HB, Johnson IM, Jones KR, Reiner A. Effect of early embryonic deletion of huntingtin from pyramidal neurons on the development and long-term survival of neurons in cerebral cortex and striatum. *Neurobiol Dis* 2018; 111: 102-117.

Franich NR, Hickey MA, Zhu C, Osborne GF, Ali N, Chu T, Bove NH, Lemesre V, Lerner RP, Zeitlin SO, Howland D, Neueder A, Landles C, Bates GP, Chesselet MF. Phenotype onset in Huntington's disease knock-in mice is correlated with the incomplete splicing of the mutant huntingtin gene. *J Neuro Res* 2019; 97: 1590–1605.

Fusco FR, Chen Q, Lamoreaux WJ, Figueredo-Cardenas G, Jiao Y, Coffman JA, Surmeier DJ, Honig MG, Carlock LR, Reiner A. Cellular localization of Huntingtin in striatal and cortical neurons in rats: Lack of correlation with neuronal vulnerability in Huntington's disease. *J Neurosci* 1999; 19: 1189-1202.

Glass M, Dragunow M, Faull RLM. The pattern of neurodegeneration in Huntington's disease: a comparative study of cannabinoid, dopamine, adenosine and GABAA receptor alterations in the human basal ganglia in Huntington's disease. *Neuroscience* 2000; 97: 505–519.

Gu X, Cantle JP, Greiner ER, Lee CY, Barth AM, Gao F, Park CS, Zhang Z, Sandoval-Miller S, Zhang RL, Diamond M, Mody I, Coppola G, Yang XW. N17 modifies mutant huntingtin nuclear pathogenesis and severity of disease in HD BAC transgenic mice. *Neuron* 2015; 85, 726–741.

Gutekunst CA, Li SH, Yi H, Mulroy JS, Kuemmerle S, Jones R, Rye D, Ferrante RJ, Hersch SM, Li XJ. Nuclear and neuropil aggregates in Huntington's disease: relationship to neuropathology. *J Neurosci* 1999; 19: 2522–2534.

Handsaker RE, Kashin S, Reed Nm, Tan S, Lee WS, McDonald TM, Morris K, Kamitaki N, Mullally CD, Morakabati NR, Goldman M, Lind G, Kohli R, Lawton E, Hogan M, Ichihara K, Berretta S, McCarroll SS. Long somatic DNA-repeat expansion drives neurodegeneration in Huntington's disease. *Cell* 2025; 188: 623-639.

Hausmann FS, Barrett JM, Martin ME, Zhan H, Shepherd GMG. Axonal barcode analysis of pyramidal tract projections from mouse forelimb M1 and M2. *J Neurosci* 2022; 42: 7733–7743.

Heikkinen T, Lehtimäki K, Vartiainen N, Puoliväli J, Hendricks SJ, Glaser JR, Bradaia A, Wadel K, Touller C, Kontkanen O, Yrjänheikki JM, Buisson B, Howland D, Beaumont V, Munoz-Sanjuan I, Park LC. Characterization of neurophysiological and behavioral changes, MRI brain volumetry and 1H MRS in zQ175 knock-in mouse model of Huntington's disease. *PLoS One* 2012; 7: e50717.

Honig MG, Dorian CC, Worthen JD, Micetich AC, Mulder IA, Sanchez KB, Pierce WF, Del Mar NA, Reiner A. Progressive long-term spatial memory loss following repeat concussive and subconcussive brain injury in mice, associated with dorsal hippocampal neuron loss, microglial phenotype shift, and vascular abnormalities. *Eur J Neurosci* 2021; 54: 5844-5879.

Jiao Y, Sun Z, Lee T, Fusco FR, Kimble TD, Meade CA, Cuthbertson S, Reiner A. A simple and sensitive antigen retrieval method for free-floating and slide-mounted tissue sections. *J Neurosci Methods* 1999; 93: 149–162.

Ko J, Ou S, Patterson PH. New anti-huntingtin monoclonal antibodies: Implications for huntingtin conformation and its binding proteins. *Brain Res Bull* 2001; 56: 319-329.

Ko J, Isas JM, Sabbaugh A, Yoo JH, Pandey NK, Chongtham A, Ladinsky M, Wu WL, Rohweder H, Weiss A, Macdonald D, Munoz-Sanjuan I, Langen R, Patterson PH, Khoshnan A. Identification of distinct conformations associated with monomers and fibril assemblies of mutant huntingtin. *Human Mol Gen* 2018; 27: 2330-2343.

Kuemmerle S, Gutekunst CA, Klein AM, Li XJ, Li SH, Beal MF, Hersch SM, Ferrante RJ. Huntington aggregates may not predict neuronal death in Huntington's disease. *Ann Neurol* 1999; 46: 842-849.

Landles C, Sathasivam K, Weiss A, Woodman B, Moffitt H, Finkbeiner S, Sun B, Gafni J, Ellerby LM, Trottier Y, Richards WG, Osmand A, Paganetti P, Bates GP. Proteolysis of mutant huntingtin produces an exon 1 fragment that accumulates as an aggregated protein in neuronal nuclei in Huntington disease. *J Biol Chem* 2010; 285: 8808-8823.

Lei W, Jiao Y, Del Mar N, Reiner A. Evidence for differential cortical input to direct pathway versus indirect pathway striatal projection neurons in rats. *J Neurosci* 2004; 24: 8289-8299.

Mätlik K, Baffuto M, Kus L, Deshmukh AL, Davis DA, Paul MR, Carroll TS, Caron MC, Masson JY, Pearson CE, Heintz N. Cell type specific CAG repeat expansions and toxicity of mutant huntingtin in human striatum and cerebellum. *Nature Genetics* 2024; 56: 383-394.

Maat-Schieman ML, Dorsman JC, Smoor MA, Siesling S, Van Duinen SG, Verschuuren JJ, den Dunnen JT, Van Ommen GJ, Roos RA. Distribution of inclusions in neuronal nuclei and dystrophic neurites in Huntington disease brain. *J Neuropathol Exp Neurol* 1999; 58: 129–137.

Massouh M, Wallman, Pourcher E, MJ, Parent A. The fate of the large striatal interneurons expressing calretinin in huntington's disease. *Neuroscience Research* 2008; 62: 216-224.

Meade CA, Deng YP, Fusco FR, Del Mar N, Hersch S, Goldowitz D, Reiner A. Cellular localization and development of neuronal intranuclear inclusions in striatal and cortical neurons in R6/2 transgenic mice. *J Com Neurol* 2002; 449: 241-269.

Menalled LB, Kudwa AE, Miller S, Fitzpatrick J, Watson-Johnson J, Keating N, Ruiz M, Mushlin R, Alosio W, McConnell K, Connor D, Murphy C, Oakeshott S, Kwan M, Beltran J, Ghavami A, Brunner D, Park LC, Ramboz S, Howland D. Comprehensive behavioral and molecular characterization of a new knock-in mouse model of Huntington's disease: zQ175. *PLoS One* 2012; 7: e49838.

Menalled L, Lutz C, Ramboz S, Brunner D, Lager B, Noble S, Park L, Howland D. *A Field Guide to Working with Mouse Models of Huntington's Disease.* 2014. The Jackson Laboratory.

Missineo A, Tomei L, Alaimo N, Martufi P, Zavattieri M, Ferrari F, Piai A, Séguin J, Esquina C, Huang N, Wu H-Y, Nicotra E, Pace J, Doherty EM. Highly selective monoclonal antibodies targeting the HTT exon1 neo-epitope. *19th Annual Huntington's Disease Therapeutics Conference* (HDTC), Palm Springs, CA 2024.

Nana AL, Kim EH, Thu DC, Oorschot DE, Tippett LJ, Hogg VM, Synek BJ, Roxburgh R, Waldvogel HJ, Faull RL. Widespread heterogeneous neuronal loss across the cerebral cortex in Huntington's Disease. *Journal of Huntington's Disease* 2014; 3:45–64.

Neueder A, Landles C, Ghosh R, Howland D, Myers RH, Faull RLM, Tabrizi SJ, Bates GP. The pathogenic exon 1 HTT protein is produced by incomplete splicing in Huntington's disease patients. *Sci Rep* 2017; 7: 1307.

Pressl C, Mätlik K, Kus L, Darnell P, Luo JD, Paul MR, Weiss AR, Liguore W, Carroll TS, Davis DA, McBride J, Heintz N. Selective vulnerability of layer 5a corticostriatal neurons in Huntington's disease. *Neuron* 2024; 112: 1–18.

Reiner A, Albin RL, Anderson KD, D'Amato CJ, Penney JB, Young AB. Differential loss of striatal projection neurons in Huntington's disease. *Proc Natl Acad Sci USA* 1988; 85: 5733-5737.

Reiner A, Jiao Y, Del mar N, Laverghetta AV, Lei WL. Differential morphology of pyramidal tract-type and intratelencephalically projecting-type corticostriatal neurons and their intrastriatal terminals in rats. *J Comp Neurol* 2003; 457: 420-440.

Reiner A, Del Mar N, Deng YP, Meade CA, Sun Z, Goldowitz D. R6/2 Neurons with intranuclear inclusions survive for prolonged periods in the brains of chimeric mice. *J Comp Neurol* 2007; 505: 603-629.

Reiner A, Dragatsis I, Dietrich P. Genetics and neuropathology of Huntington's disease. *Int Rev Neurobiol* 2011; 98: 325–372.

Reiner A, Lafferty DC, Wang HB, Del Mar N, Deng YP. The group 2 metabotropic glutamate receptor agonist LY379268 rescues neuronal, neurochemical and motor abnormalities in R6/2 Huntington's disease mice. *Neurobiol Dis* 2012; 47: 75-91.

Reiner A, Shelby E, Wang H, DeMarch Z, Deng Y, Guley NH, Hogg V, Roxburgh R, Tippett LJ, Waldvogel HJ, Faull RL. Striatal parvalbuminergic neurons are lost in Huntington's Disease: Implications for dystonia. *Movement Disorders* 2013; 28:1691-1699.

Richfield EK, Vonsattel JP, MacDonald ME, Sun Z, Deng YP, Reiner A. Selective loss of striatal preprotachykinin neurons in a phenocopy of Huntington's disease. *Movement Disorders* 2002; 17: 327-332.

Sapp E, Boudi A, Iwanowicz A, Belgrad J, Miller R, O'Reilly D, Yamada K, Deng Y, Joni M, Li X, Kegel-Gleason K, Khvorova A, Reiner A, Aronin N, DiFiglia M. Detection of httex1p by western blot and immunostaining of HD human and mouse brain using neo-epitope antibody P90 highlights impact of CAG repeat expansion on its size, solubility, and response to MSH3 silencing. *bioRxiv* 2025. 12.31.630891.

Sathasivam K, Neueder A, Gipson TA, Landles C, Benjamin AC, Bondulich MK, Smith DL, Faull RL, Roos RA, Howland D, Detloff PJ, Housman DE, Bates GP. Aberrant splicing of HTT generates the pathogenic exon 1 protein in Huntington disease. *Proc Natl Acad Sci USA* 2013; 110: 2366-2370.

Schilling G, Becher MW, Sharp AH, Jinnah HA, Duan K, Kotzuk JA, Slunt HH, Ratovitski T, Cooper JK, Jenkins NA, Copeland NG, Price DL, Ross CA, Borchelt DR. Intranuclear inclusions and neuritic aggregates in transgenic mice expressing a mutant N-terminal fragment of huntingtin. *Human Mol Genet* 1999; 8: 397-407.

Smith EJ, Sathasivam K, Landles C, Osborne GF, Mason MA, Gomez-Paredes C, Taxy BA, Milton RE, Ast A, Schindler F, Zhang C, Duan W, Wanker EE, Bates GP. Early detection of exon 1 huntingtin aggregation in zQ175 brains by molecular and histological approaches. *Brain Communications* 2023; 5: fcad010.

Sorensen SA, Bernard A, Menon V, Royall JJ, Glattfelder KJ, Desta T, Hirokawa K, Mortrud M, Miller JA, Zeng H, Hohmann JG, Jones AR, Lein ES. Correlated gene expression and target

specificity demonstrate excitatory projection neuron diversity. *Cerebral Cortex* 2015; 25: 433-449.

Spargo E, Everall IP, Lantos PL. Neuronal loss in the hippocampus in Huntington's disease: a comparison with HIV infection. *Journal of Neurology, Neurosurgery, and Psychiatry* 1993; 56: 487-491.

Thu DC, Oorschot DE, Tippett LJ, Nana AL, Hogg VM, Synek BJ, Luthi-Carter R, Waldvogel HJ, Faull RL. Cell loss in the motor and cingulate cortex correlates with symptomatology in Huntington's disease. *Brain* 2010; 133: 1094–1110.

Vonsattel JP, Myers RH, Stevens TJ, Ferrante RJ, Bird ED, Richardson EP. Neuropathological classification of Huntington's disease. *J Neuropathol Exp Neurol* 1985; 44: 559 –577.

Waelter S, Boeddrich A, Lurz R, Scherzinger E, Lueder G, Lehrach H, Wanker EE. Accumulation of mutant huntingtin fragments in aggresome-like inclusion bodies as a result of insufficient protein degradation. *Molecular Biology of the Cell* 2001; 12: 1393–1407.

Wang EN, Tydlacka S, Orr AL, Yang SH, Graham RK, Hayden MR, Li S, Chan AWS, Li XJ. Accumulation of N-terminal mutant huntingtin in mouse and monkey models implicated as a pathogenic mechanism in Huntington's disease. *Human Mol Gen* 2008; 17: 2738–2751.

Zhao DY, Bäuerlein FJB, Saha I, Hartl FU, Baumeister W, Wilfling F. Autophagy preferentially degrades non-fibrillar polyQ aggregates. *Molecular Cell* 2024; 84: 1980–1994.

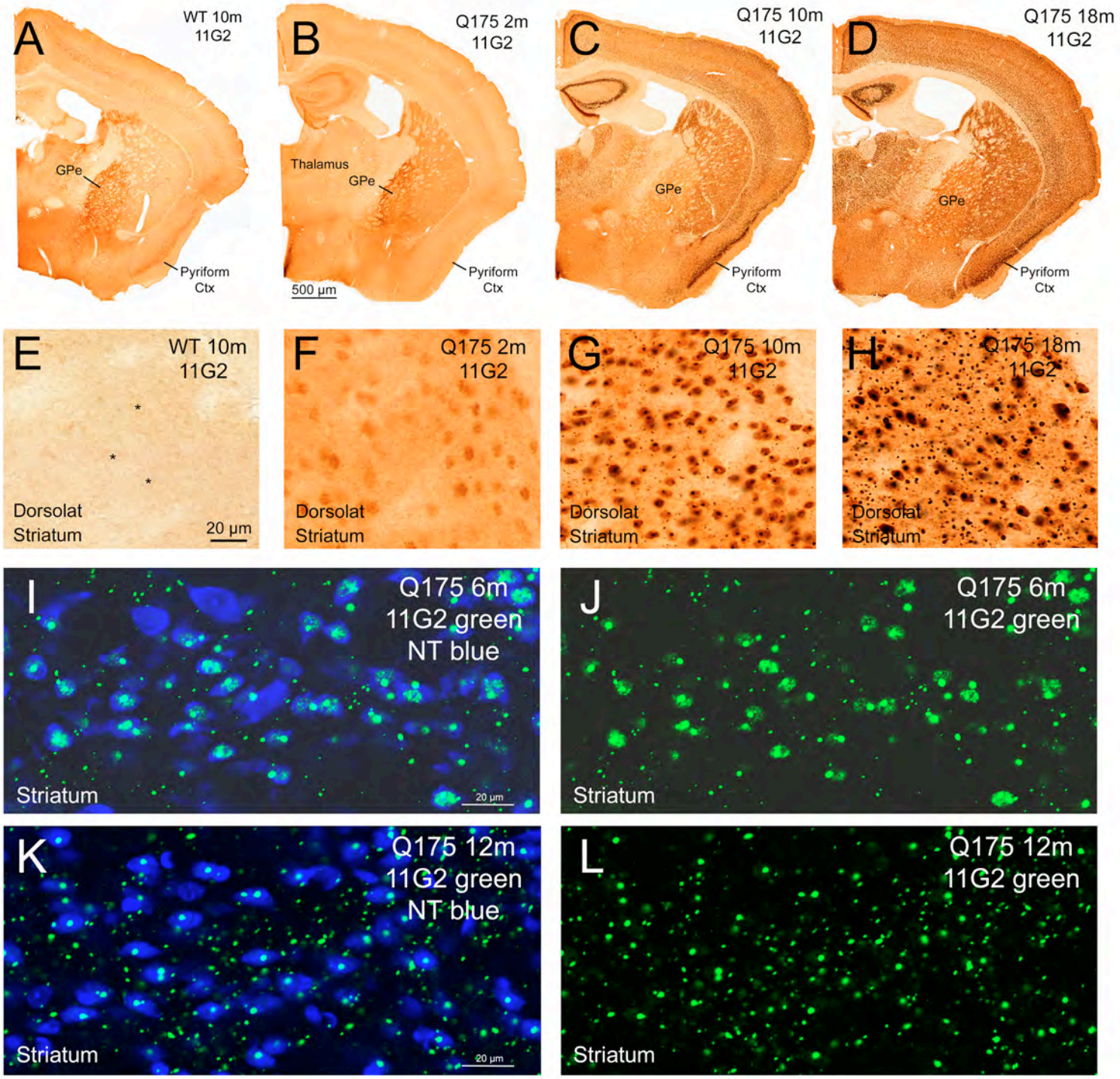
A
WT 10m
11G2
GPe
Pyriform
Ctx
B
Q175 2m
11G2
Thalamus
GPe
500 µm
Pyriform
Ctx
C
Q175 10m
11G2
GPe
Pyriform
Ctx
D
Q175 18m
11G2
GPe
Pyriform
Ctx
E
WT 10m
11G2
Dorsolat
Striatum
20 µm
F
Q175 2m
11G2
Dorsolat
Striatum
G
Q175 10m
11G2
Dorsolat
Striatum
H
Q175 18m
11G2
Dorsolat
Striatum
I
Q175 6m
11G2 green
NT blue
Striatum
20 µm
J
Q175 6m
11G2 green
Striatum
K
Q175 12m
11G2 green
NT blue
Striatum
20 µm
L
Q175 12m
11G2 green
Striatum

Figure 1

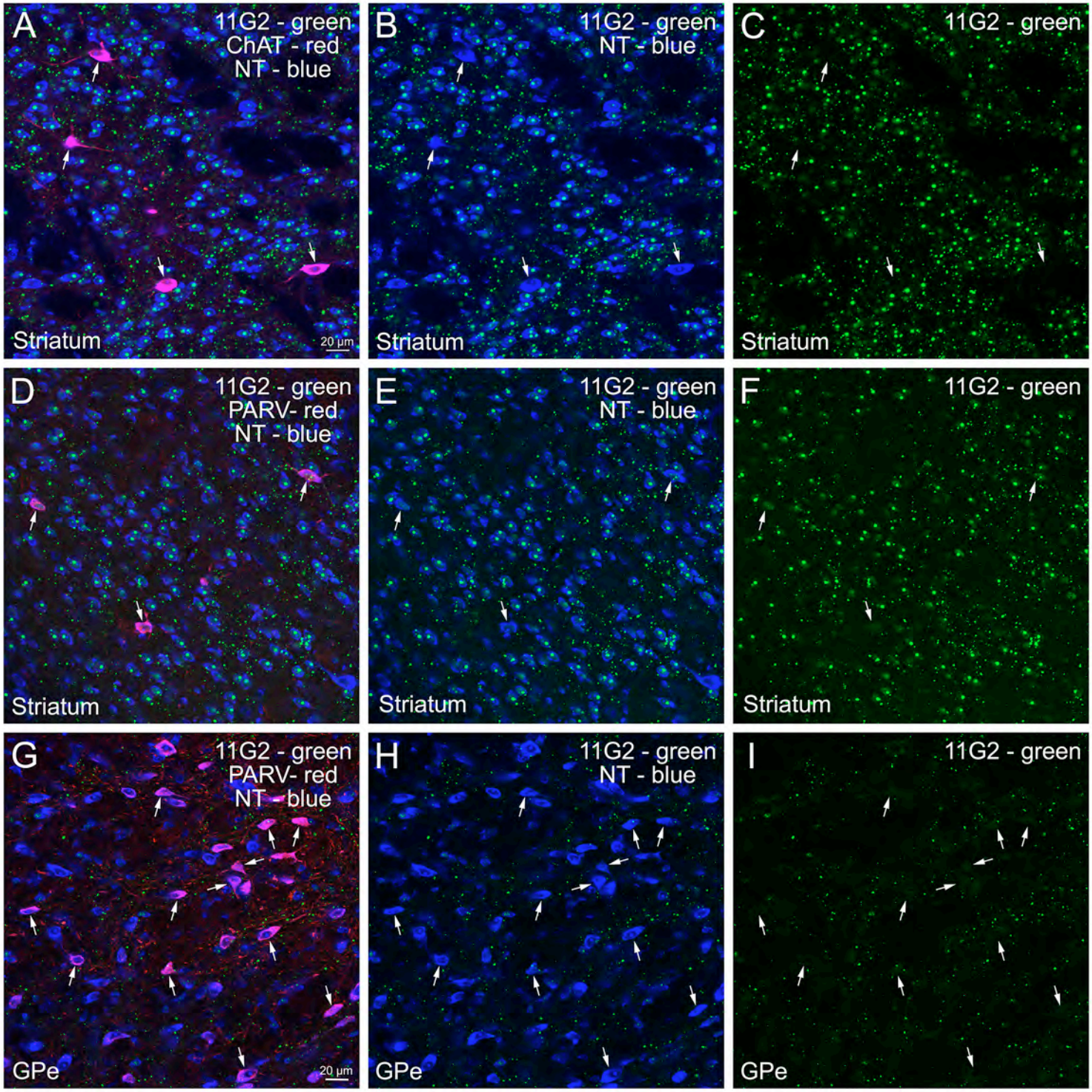
A
11G2 - green
ChAT - red
NT - blue
Striatum
20 µm
B
11G2 - green
NT - blue
Striatum
C
11G2 - green
Striatum
D
11G2 - green
PARV- red
NT - blue
Striatum
E
11G2 - green
NT - blue
Striatum
F
11G2 - green
Striatum
G
11G2 - green
PARV- red
NT - blue
GPe
20 µm
H
11G2 - green
NT - blue
GPe
I
11G2 - green
GPe

Figure 2

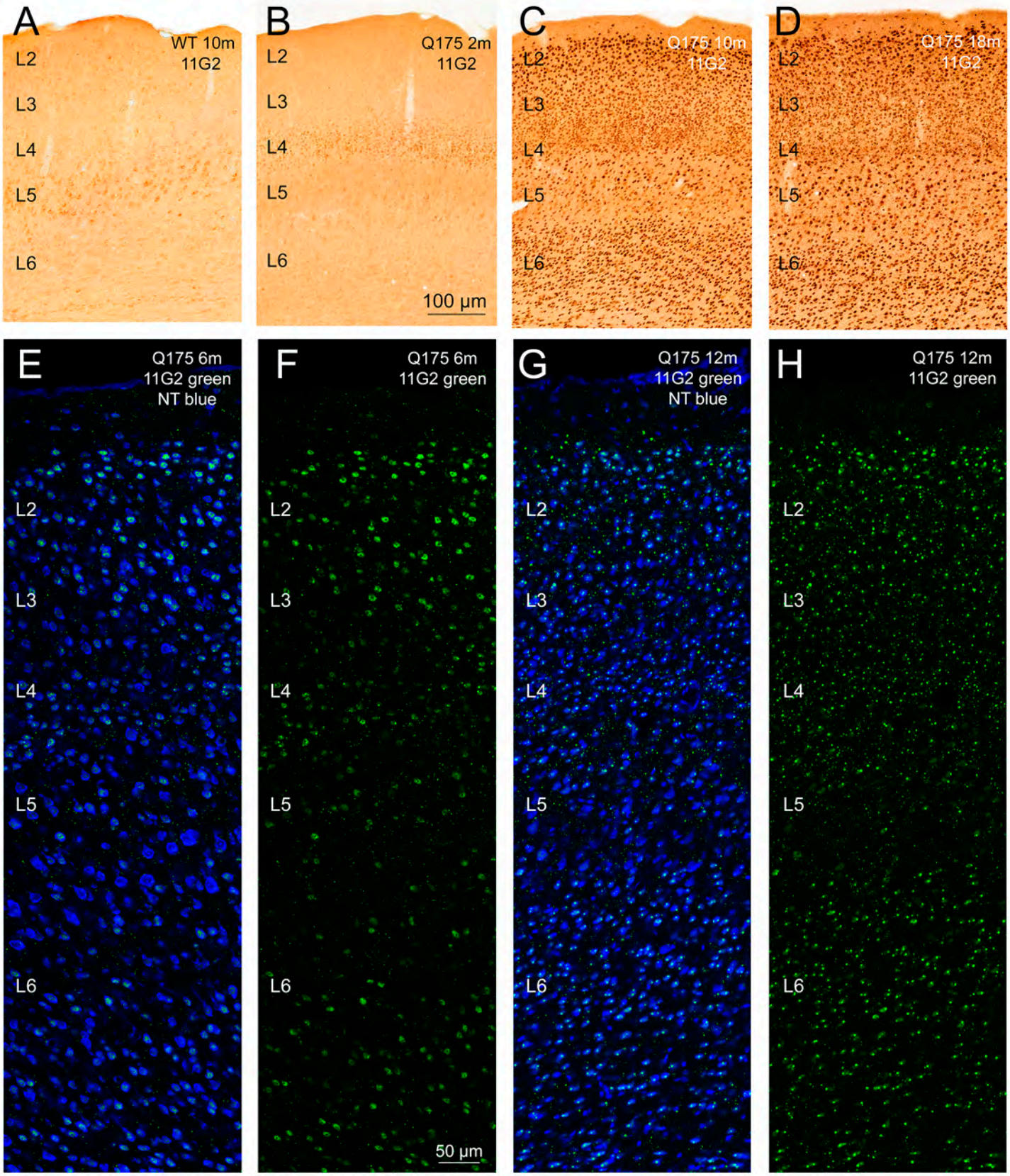
A
WT 10m
11G2
L2
L3
L4
L5
L6
B
Q175 2m
11G2
L2
L3
L4
L5
L6
100 µm
C
Q175 10m
11G2
L2
L3
L4
L5
L6
D
Q175 18m
11G2
L2
L3
L4
L5
L6
E
Q175 6m
11G2 green
NT blue
L2
L3
L4
L5
L6
F
Q175 6m
11G2 green
L2
L3
L4
L5
L6
50 µm
G
Q175 12m
11G2 green
NT blue
L2
L3
L4
L5
L6
H
Q175 12m
11G2 green
L2
L3
L4
L5
L6

Figure 3

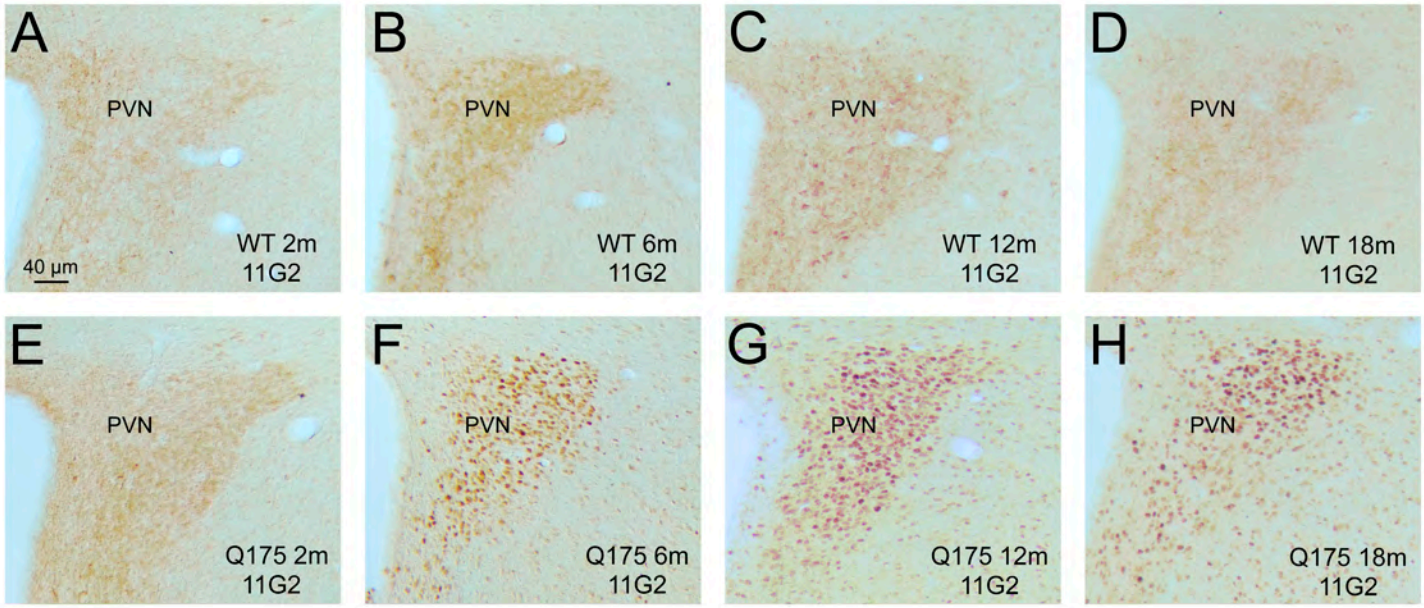
A
PVN
40 µm
WT 2m
11G2
B
PVN
WT 6m
11G2
C
PVN
WT 12m
11G2
D
PVN
WT 18m
11G2
E
PVN
Q175 2m
11G2
F
PVN
Q175 6m
11G2
G
PVN
Q175 12m
11G2
H
PVN
Q175 18m
11G2

Figure 4

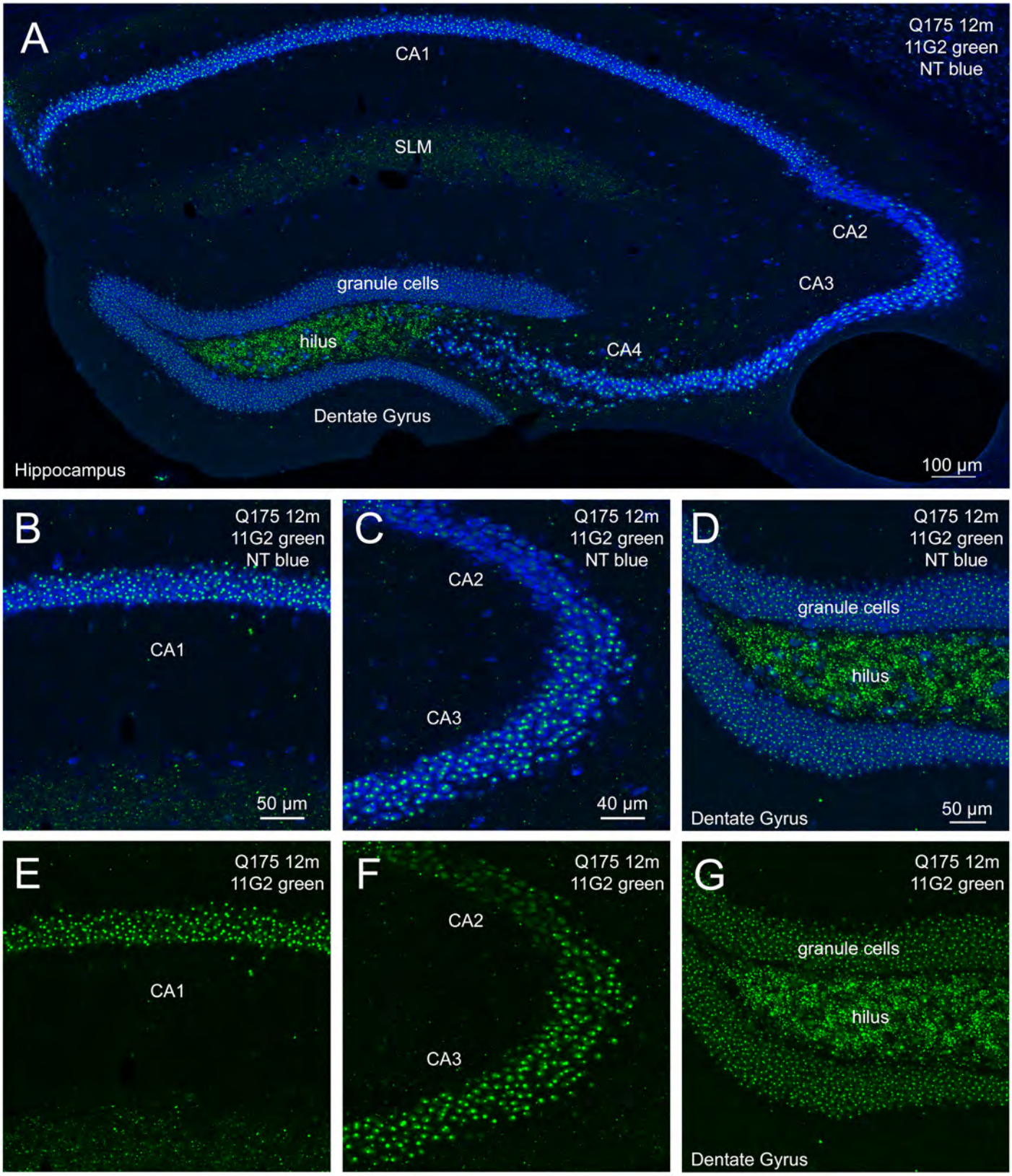
A
Q175 12m
11G2 green
NT blue
CA1
SLM
CA2
CA3
granule cells
hilus
CA4
Dentate Gyrus
Hippocampus
100 µm
B
Q175 12m
11G2 green
NT blue
CA1
50 µm
C
Q175 12m
11G2 green
NT blue
CA2
CA3
40 µm
D
Q175 12m
11G2 green
NT blue
granule cells
hilus
Dentate Gyrus
50 µm
E
Q175 12m
11G2 green
CA1
F
Q175 12m
11G2 green
CA2
CA3
G
Q175 12m
11G2 green
granule cells
hilus
Dentate Gyrus

Figure 5

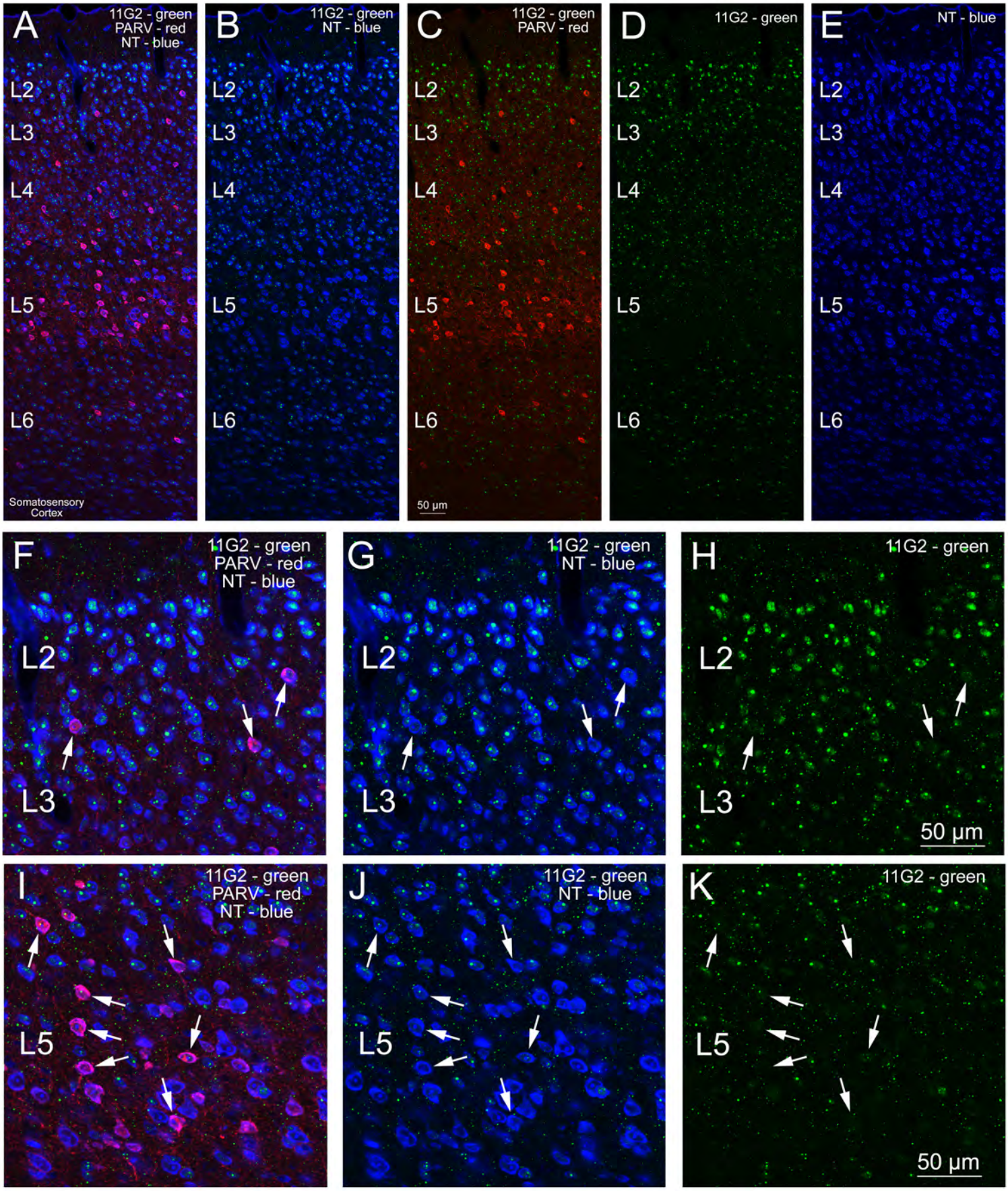
A
11G2 - green
PARV - red
NT - blue
L2
L3
L4
L5
L6
Somatosensory Cortex
B
11G2 - green
NT - blue
C
11G2 - green
PARV - red
50 µm
D
11G2 - green
E
NT - blue
F
G
H
I
J
K

Figure 6

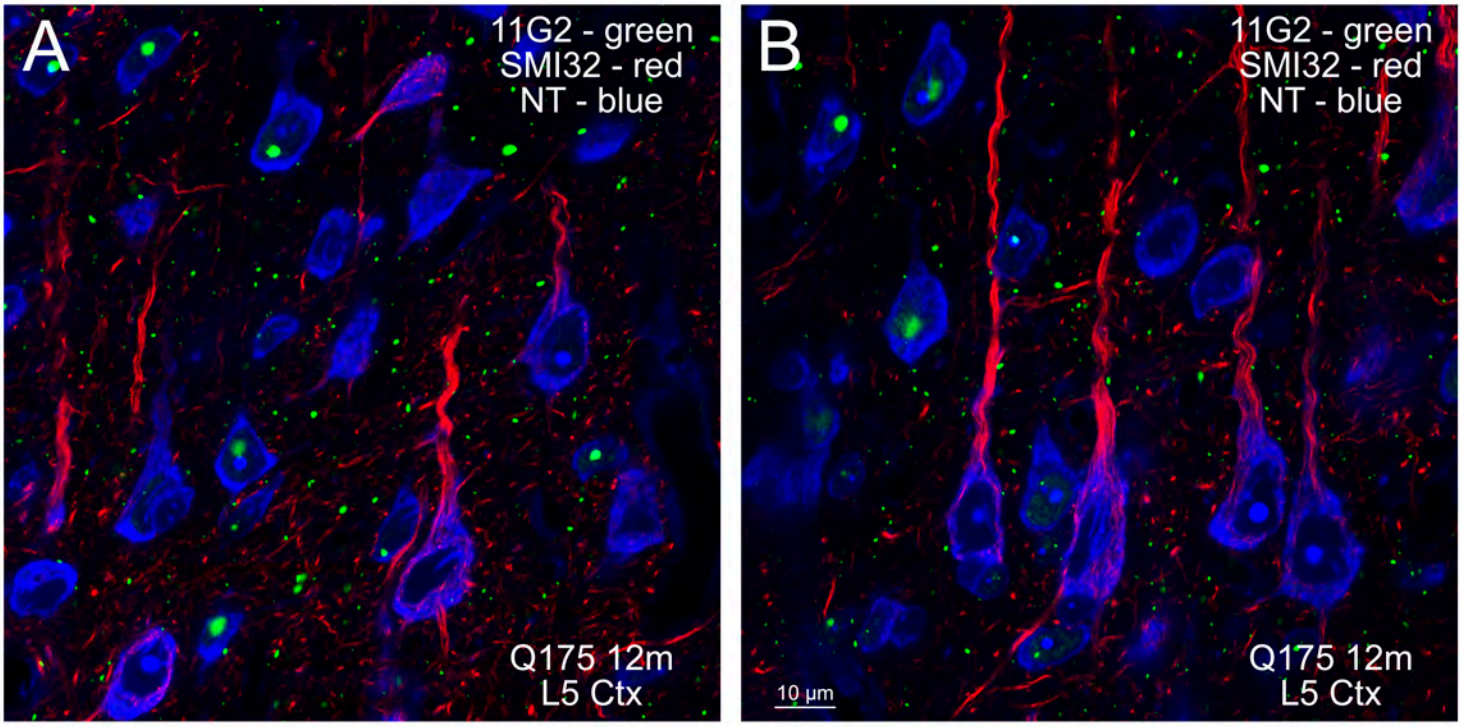
A
11G2 - green
SMI32 - red
NT - blue
Q175 12m
L5 Ctx
B
11G2 - green
SMI32 - red
NT - blue
Q175 12m
L5 Ctx
10 µm

Figure 7

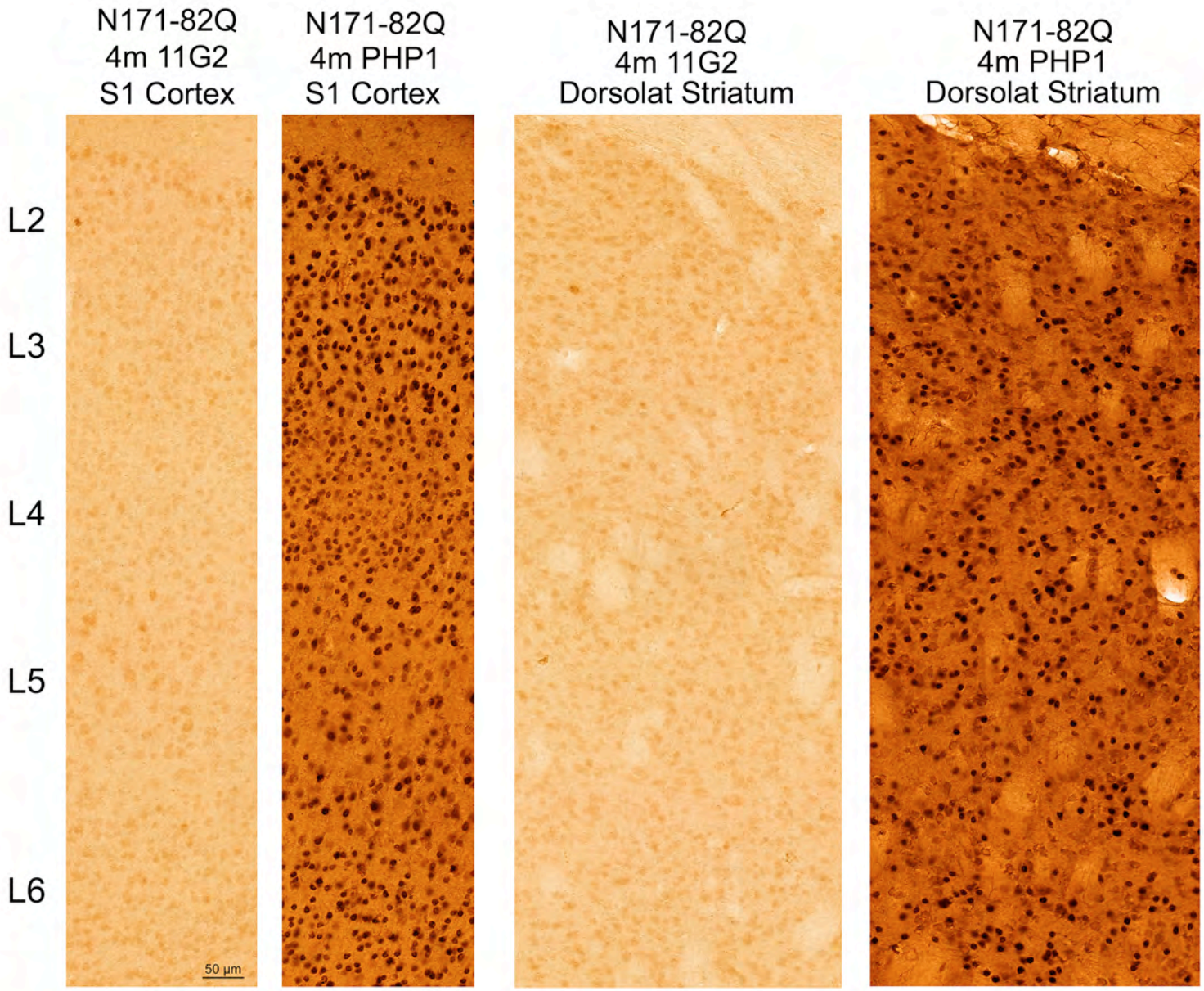
N171-82Q
4m 11G2
S1 Cortex
N171-82Q
4m PHP1
S1 Cortex
N171-82Q
4m 11G2
Dorsolat Striatum
N171-82Q
4m PHP1
Dorsolat Striatum
L2
L3
L4
L5
L6
50 µm

Figure 8

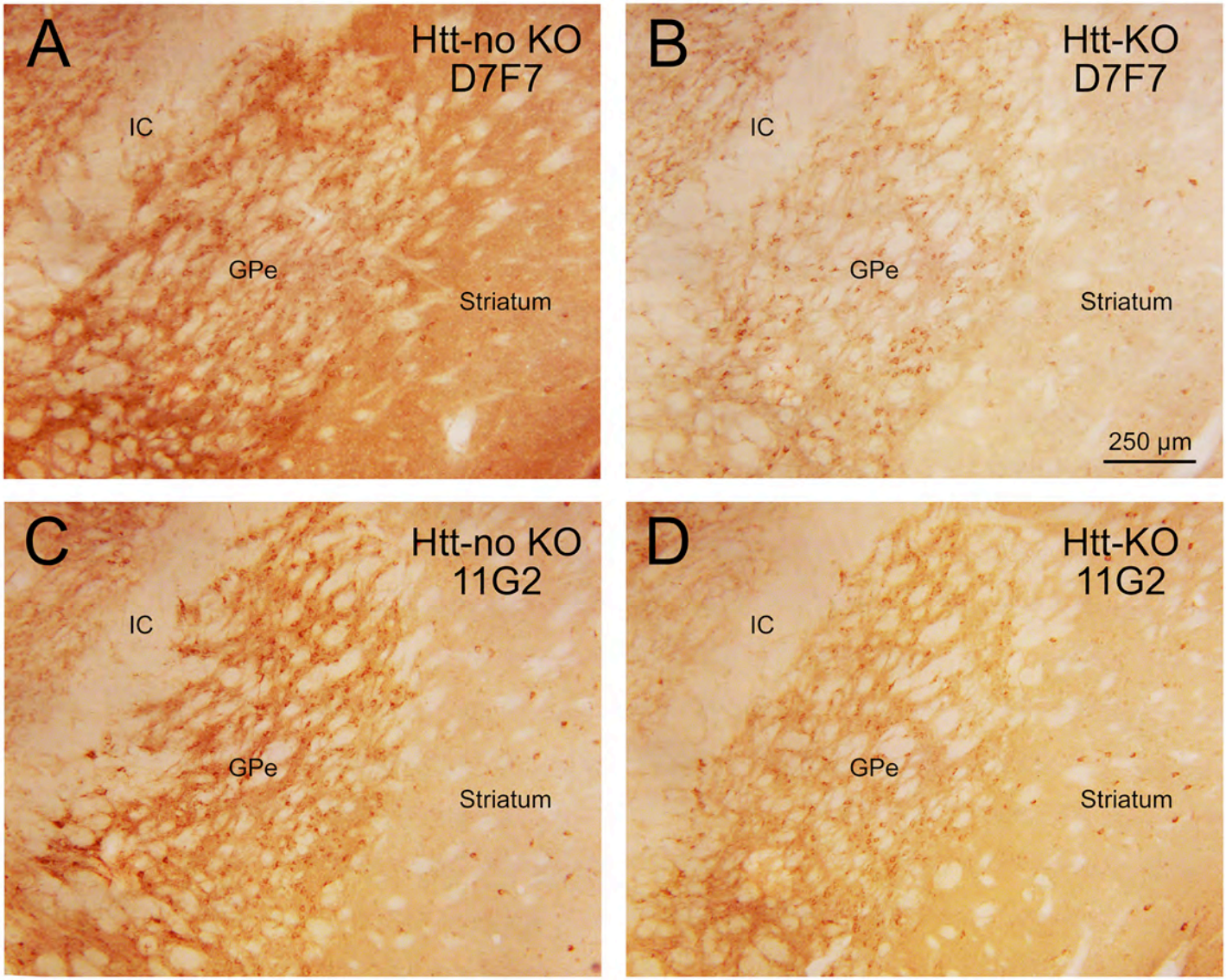
A
Htt-no KO
D7F7
IC
GPe
Striatum
B
Htt-KO
D7F7
IC
GPe
Striatum
250 µm
C
Htt-no KO
11G2
IC
GPe
Striatum
D
Htt-KO
11G2
IC
GPe
Striatum

Figure 9

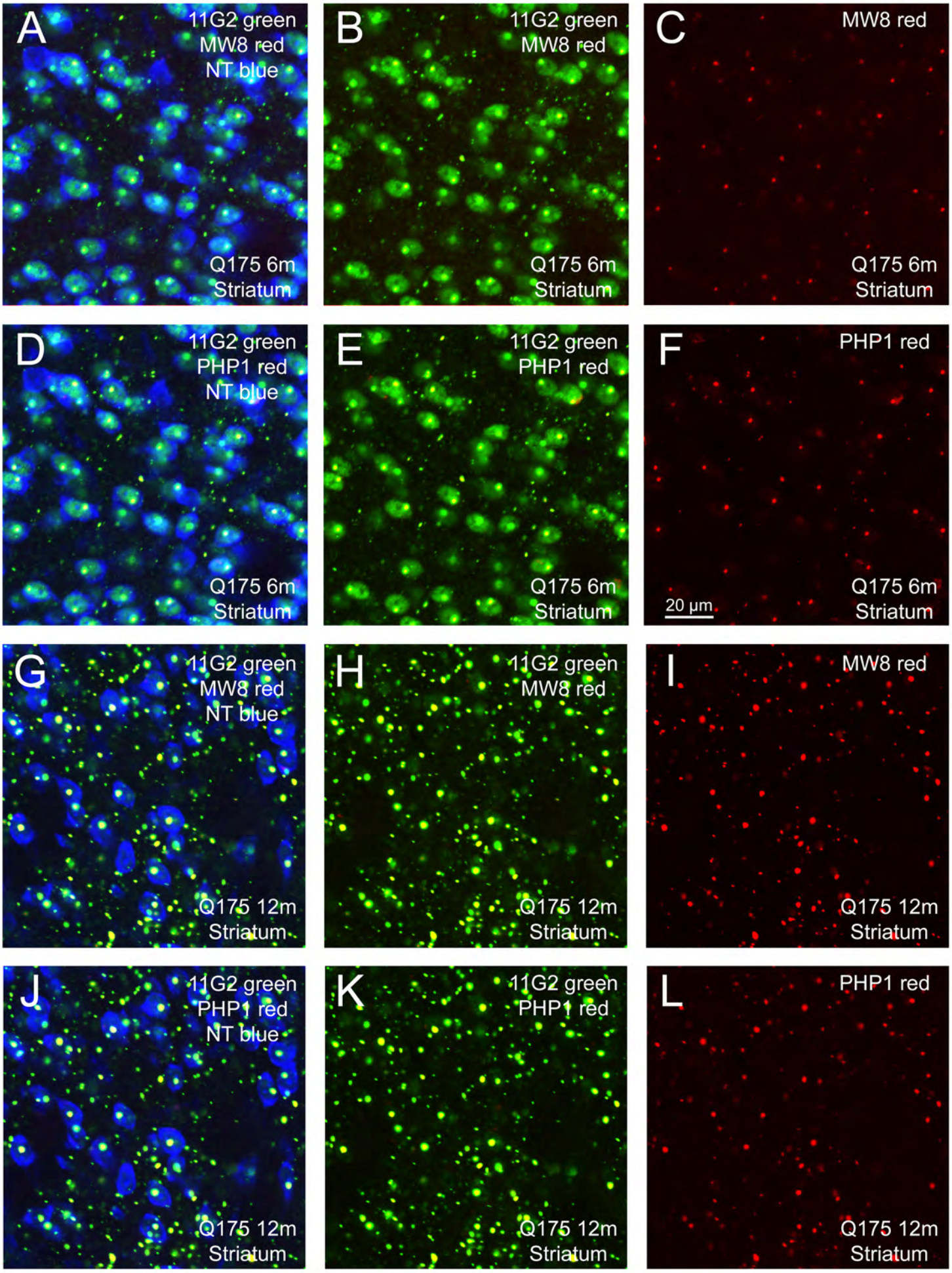
A
11G2 green
MW8 red
NT blue
Q175 6m
Striatum
B
11G2 green
MW8 red
Q175 6m
Striatum
C
MW8 red
Q175 6m
Striatum
D
11G2 green
PHP1 red
NT blue
Q175 6m
Striatum
E
11G2 green
PHP1 red
Q175 6m
Striatum
F
PHP1 red
20 µm
Q175 6m
Striatum
G
11G2 green
MW8 red
NT blue
Q175 12m
Striatum
H
11G2 green
MW8 red
Q175 12m
Striatum
I
MW8 red
Q175 12m
Striatum
J
11G2 green
PHP1 red
NT blue
Q175 12m
Striatum
K
11G2 green
PHP1 red
Q175 12m
Striatum
L
PHP1 red
Q175 12m
Striatum

Figure 10

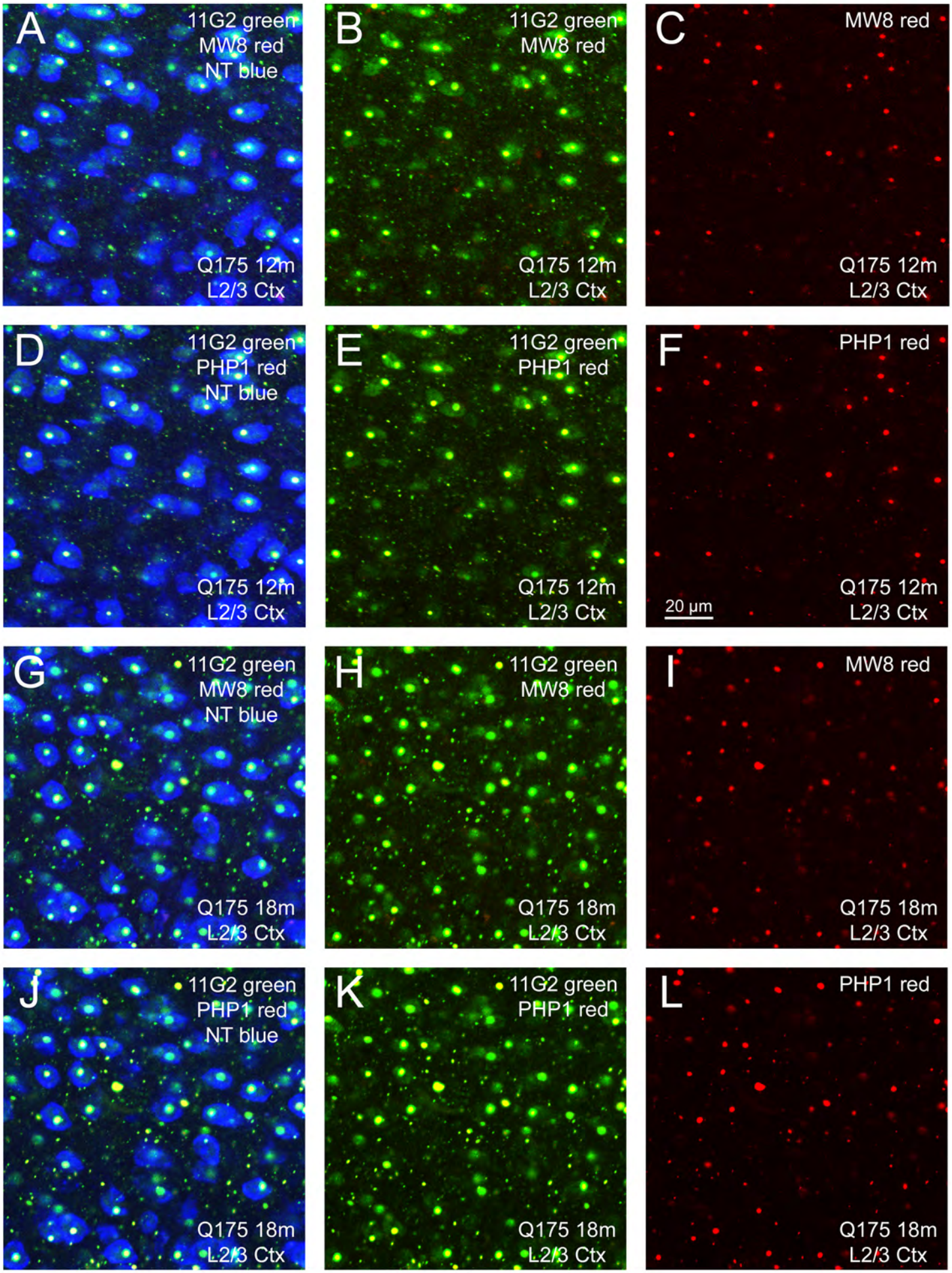
A
11G2 green
MW8 red
NT blue
Q175 12m
L2/3 Ctx
B
11G2 green
MW8 red
Q175 12m
L2/3 Ctx
C
MW8 red
Q175 12m
L2/3 Ctx
D
11G2 green
PHP1 red
NT blue
Q175 12m
L2/3 Ctx
E
11G2 green
PHP1 red
Q175 12m
L2/3 Ctx
F
PHP1 red
20 µm
Q175 12m
L2/3 Ctx
G
11G2 green
MW8 red
NT blue
Q175 18m
L2/3 Ctx
H
11G2 green
MW8 red
Q175 18m
L2/3 Ctx
I
MW8 red
Q175 18m
L2/3 Ctx
J
11G2 green
PHP1 red
NT blue
Q175 18m
L2/3 Ctx
K
11G2 green
PHP1 red
Q175 18m
L2/3 Ctx
L
PHP1 red
Q175 18m
L2/3 Ctx

Figure 11

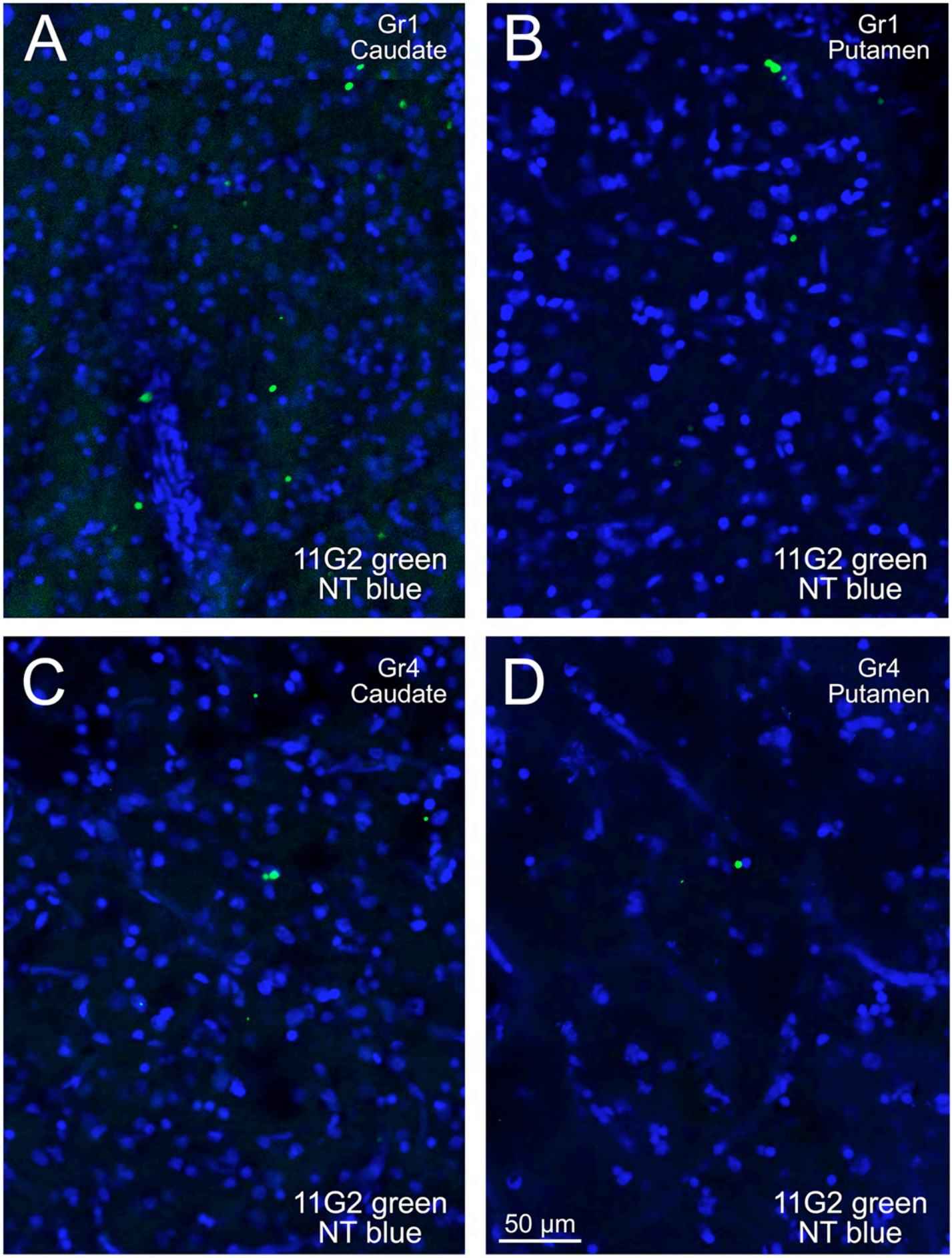
A
Gr1
Caudate
11G2 green
NT blue
B
Gr1
Putamen
11G2 green
NT blue
C
Gr4
Caudate
11G2 green
NT blue
D
Gr4
Putamen
50 µm
11G2 green
NT blue

Figure 12

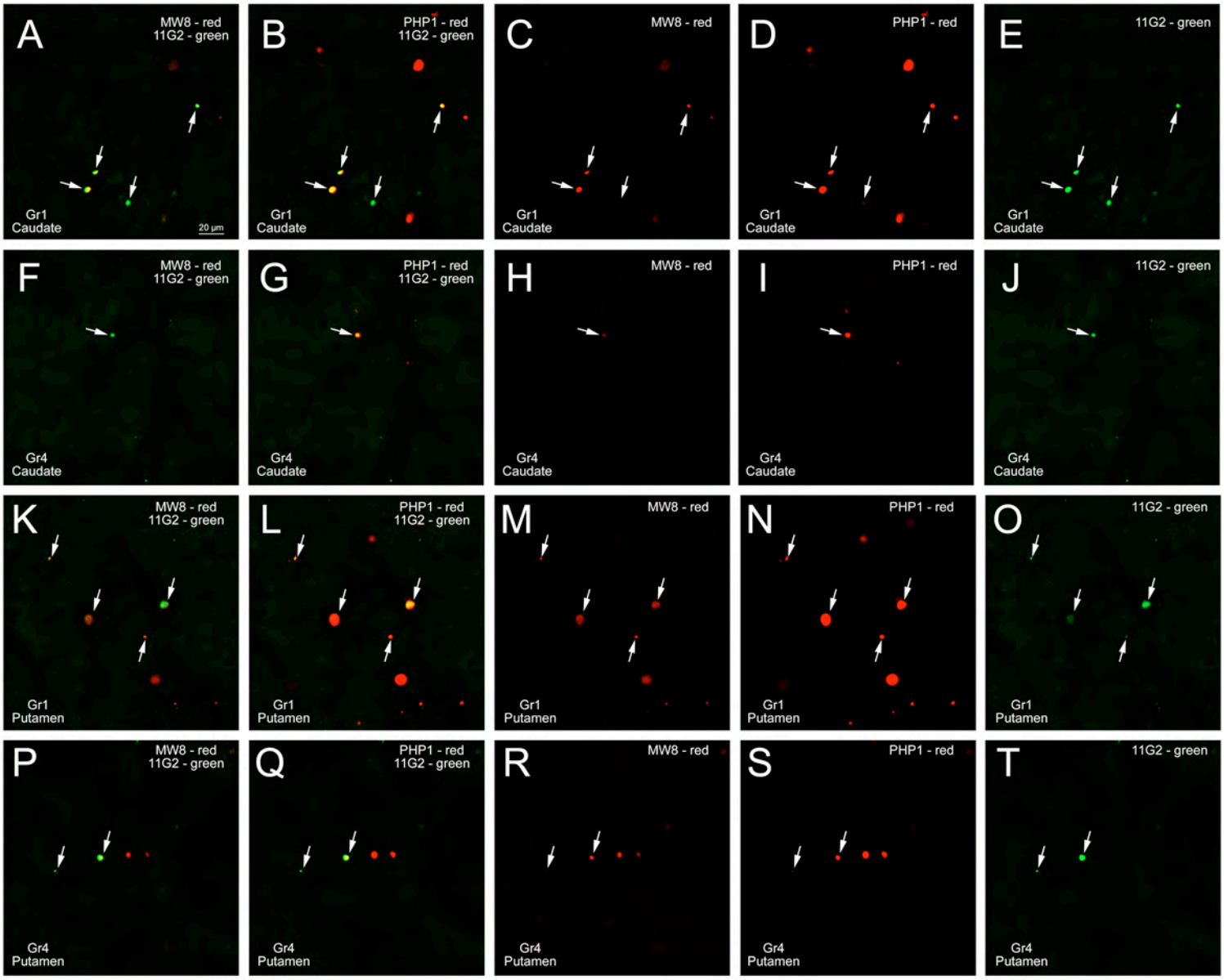
A
MW8 - red
11G2 - green
Gr1
Caudate
20 µm
B
PHP1 - red
11G2 - green
Gr1
Caudate
C
MW8 - red
Gr1
Caudate
D
PHP1 - red
Gr1
Caudate
E
11G2 - green
Gr1
Caudate
F
MW8 - red
11G2 - green
Gr4
Caudate
G
PHP1 - red
11G2 - green
Gr4
Caudate
H
MW8 - red
Gr4
Caudate
I
PHP1 - red
Gr4
Caudate
J
11G2 - green
Gr4
Caudate
K
MW8 - red
11G2 - green
Gr1
Putamen
L
PHP1 - red
11G2 - green
Gr1
Putamen
M
MW8 - red
Gr1
Putamen
N
PHP1 - red
Gr1
Putamen
O
11G2 - green
Gr1
Putamen
P
MW8 - red
11G2 - green
Gr4
Putamen
Q
PHP1 - red
11G2 - green
Gr4
Putamen
R
MW8 - red
Gr4
Putamen
S
PHP1 - red
Gr4
Putamen
T
11G2 - green
Gr4
Putamen

Figure 13

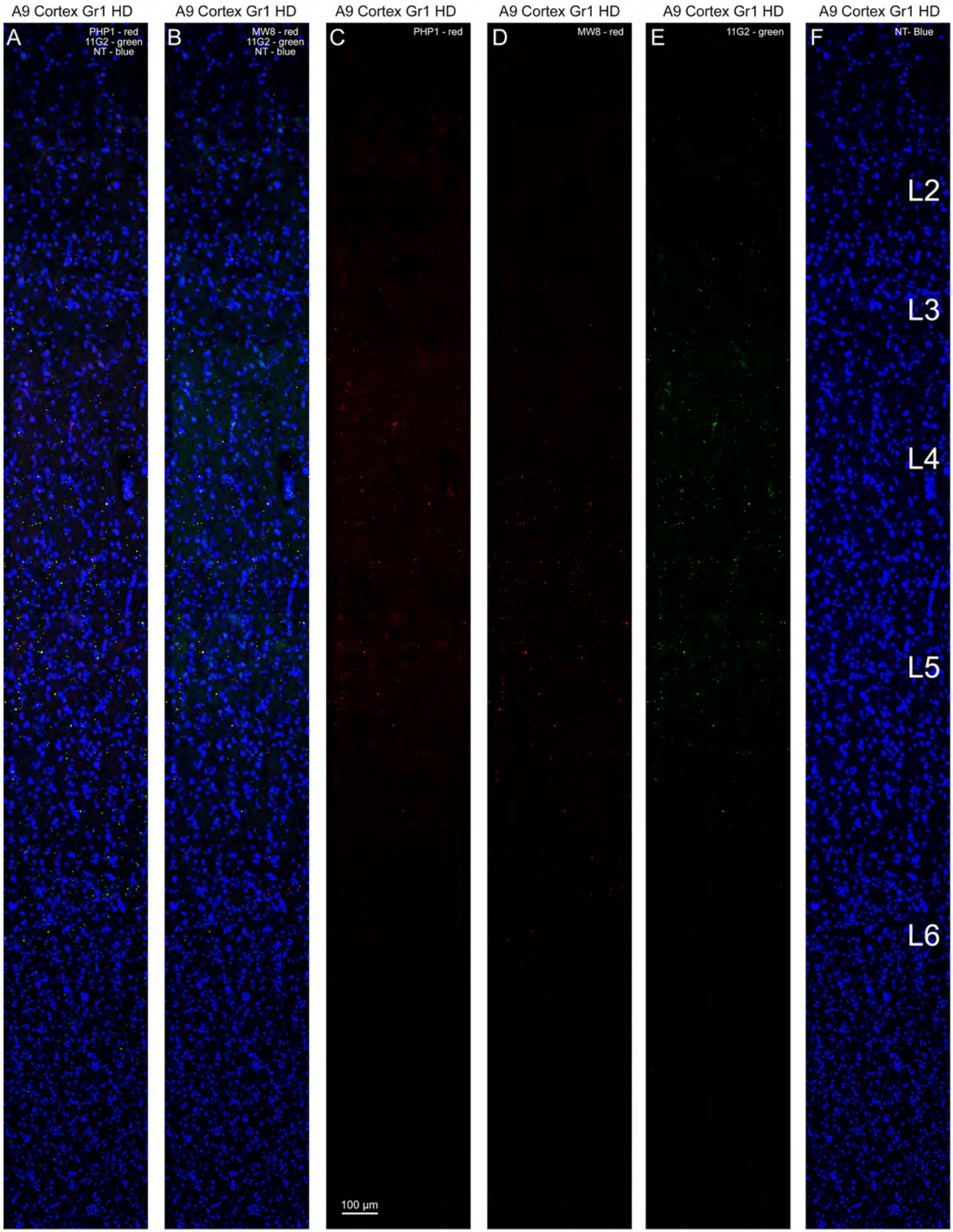
A9 Cortex Gr1 HD
A
PHP1 - red
11G2 - green
NT - blue
A9 Cortex Gr1 HD
B
MW8 - red
11G2 - green
NT - blue
A9 Cortex Gr1 HD
C
PHP1 - red
100 µm
A9 Cortex Gr1 HD
D
MW8 - red
A9 Cortex Gr1 HD
E
11G2 - green
A9 Cortex Gr1 HD
F
NT- Blue
L2
L3
L4
L5
L6

Figure 14

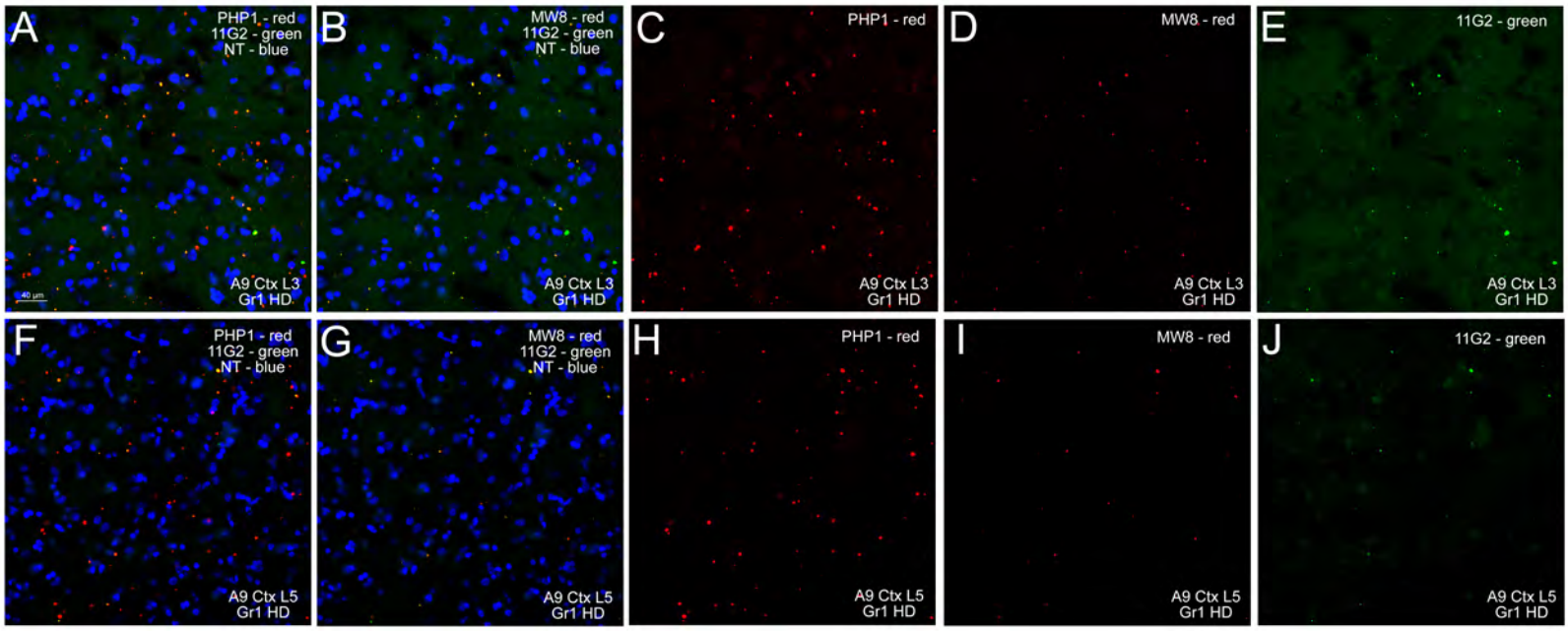
A
PHP1 - red
11G2 - green
NT - blue
A9 Ctx L3
Gr1 HD
B
MW8 - red
11G2 - green
NT - blue
A9 Ctx L3
Gr1 HD
C
PHP1 - red
A9 Ctx L3
Gr1 HD
D
MW8 - red
A9 Ctx L3
Gr1 HD
E
11G2 - green
A9 Ctx L3
Gr1 HD
F
PHP1 - red
11G2 - green
NT - blue
A9 Ctx L5
Gr1 HD
G
MW8 - red
11G2 - green
NT - blue
A9 Ctx L5
Gr1 HD
H
PHP1 - red
A9 Ctx L5
Gr1 HD
I
MW8 - red
A9 Ctx L5
Gr1 HD
J
11G2 - green
A9 Ctx L5
Gr1 HD

Figure 15

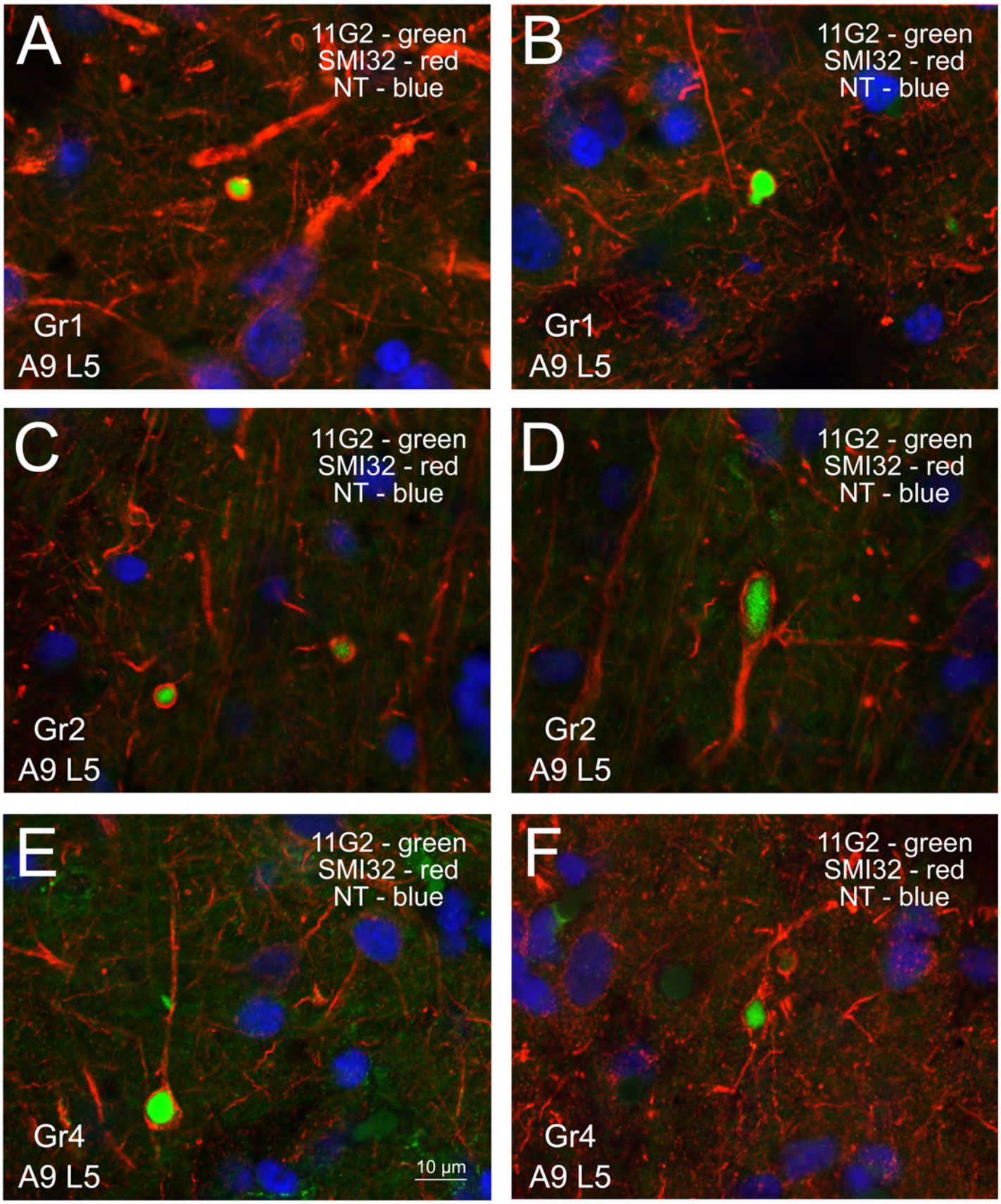
A
11G2 - green
SMI32 - red
NT - blue
Gr1
A9 L5
B
11G2 - green
SMI32 - red
NT - blue
Gr1
A9 L5
C
11G2 - green
SMI32 - red
NT - blue
Gr2
A9 L5
D
11G2 - green
SMI32 - red
NT - blue
Gr2
A9 L5
E
11G2 - green
SMI32 - red
NT - blue
Gr4
A9 L5
10 µm
F
11G2 - green
SMI32 - red
NT - blue
Gr4
A9 L5

Figure 16

Table 1

Antibody	Antigen	Catalog #	Company	Host	Antigen Retrieval Mouse	Antigen Retrieval Human	RRID
11G2	KLH conjugated - C-AEEPLHRP(OH)	N/A	CHDI	rabbit monoclonal IgG	No	Yes	None
1B12	KLH conjugated - C-AEEPLHRP(OH)	N/A	CHDI	rabbit monoclonal IgG	No	Yes	None
PHP1	aa 57-65 of human huntingtin	CHDI-90001515-2	CHDI	mouse monoclonal IgG1	No	Yes	None
MW8	human exon 1 protein with 67Q	CHDI-90000942-2	CHDI	mouse monoclonal IgG2a	No	Yes	AB_528297
D7F7	residues surrounding aa 1220 of human huntingtin	5656	Cell Signaling	rabbit monoclonal IgG	No	N/A	AB_10827977
NeuN	aa 1-100 of synthetic human NeuN	MAB377	Chemicon	mouse monoclonal IgG	No	N/A	AB_177621
ChAT	human placental ChAT	AB 144P	Millipore	goat polyclonal IgG	No	N/A	AB_2079751
PARV	carp muscle PARV	P3171	Sigma-Aldrich	mouse monoclonal IgG	No	N/A	AB_2313693
D1	97 amino acid C-terminal fragment of human D1	D-187	Sigma-Aldrich	rat monoclonal IgG	NO	N/A	AB_1840789
SMI32	nonphosphorylated 200 kD neurofilament protein	801701	BioLegend	mouse monoclonal IgG	NO	N/A	AB_2315330

Table 2

Case ID	Source	Sex	HD Grade	Age at Death	PMD
HD0-1	VU	M	0	28	6.0
HD1-1	UAB	M	1	49	18.0
HD1-2	UAB	M	1	55	21.0
HD1-3	UM	M	1	87	10.0
HD1-4	UCLA	M	1	57	15.0
HD1-5	DHRC	M	1	60	14.0
HD2-1	UAB	F	2	56	13.0
HD2-2	UR	M	2	74	16.0
HD2-3	UR	F	2	62	NA
HD2-4	UR	M	2	67	10.0
HD2-5	UR	F	2	70	6.0
HD2-6	UR	F	2	62	16.0
HD3-1	UCLA	M	3	72	15.0
GD3-2	UCLA	M	3	54	4.0
HD3-3	UR	M	3	76	18.0
HD3-4	DHRC	F	3	73	18.0
HD3-5	UM	F	3	60	12.0
HD3-6	UR	F	3	84	14.0
HD4-1	UR	F	4	52	14.0
HD4-2	UAB	F	4	70	17.0
HD4-3	UAB	F	4	58	43.0
HD4-4	UAB	F	4	78	24.0
Control		4F, 3M	Control	**63.6**	**25.4**
HD		11F, 11M	HD	**63.8**	**15.4**

Table 3

		11G2	11G2	11G2	11G2
		Load	Load	Load	Load
Mouse Region	Human Equivalent	2 mo Q175	6 mo Q175	12 mo Q175	18 mo Q175
Rostral Medial Striatum	Rostral Caudate	2.05	2.63	3.60	3.93
Rostral Lateral Striatum	Rostral Putamen	1.95	2.40	3.55	3.85
Mid Medial Striatum	Mid Caudate	1.95	2.55	3.50	3.93
Mid Lateral Striatum	Mid Putamen	1.80	2.40	3.45	3.90
Caudal Medial Striatum	Caudal Caudate	2.08	2.45	3.55	3.87
Caudal Lateral Striatum	Caudal Putamen	1.98	2.38	3.50	3.85
All Striatum	Caudo-putamen	1.97	2.47	3.53	3.89
All Caudate	Caudate	2.03	2.54	3.55	3.91
All Putamen	Putamen	1.91	2.39	3.50	3.87
Globus Pallidus Externus	Globus Pallidus Externus	0.00	0.18	0.38	1.13
Globus Pallidus Internus	Globus Pallidus Internus	0.00	0.25	0.45	0.88
SN pars Reticulata	SN pars Reticulata	0.00	0.43	0.88	1.43
Nucleus Accumbens	Nucleus Accumbens	1.83	2.50	3.40	3.72
Olfactory Tubercle	Olfactory Tubercle	1.80	2.38	3.50	3.85
Ventral Pallidum	Ventral Pallidum	0.00	0.33	0.75	0.83
CA1	CA1	2.13	2.70	4.00	4.00
CA2	CA2	0.04	0.45	3.00	3.50
CA3	CA3	1.00	2.33	3.90	3.95
CA4	CA4	1.00	2.20	3.40	3.83
Dentate Granule	Dentate Granule	0.15	2.18	4.00	4.00
Dentate Hilus	Dentate Hilus	0.25	0.88	3.55	3.93
Subiculum	Subiculum	0.50	0.88	3.13	3.28
Hippocampal Complex	Hippocampal Complex	0.72	1.66	3.57	3.78
Entorhinal Ctx	Entorhinal Ctx	0.00	1.70	3.00	3.40
Pyriform Ctx	Pyriform Ctx	0.00	2.63	3.50	4.00
Basolateral Amygdala	Basolateral Amygdala	0.25	1.38	1.83	2.50
Basomedial Amygdala	Basomedial Amygdala	0.05	0.55	1.78	1.50
Central Amygdala	Central Amygdala	0.55	1.25	2.75	2.75
Medial Amygdala	Medial Amygdala	0.30	0.30	1.13	1.50
Cortical Amygdala	Cortical Amygdala	0.30	0.55	1.88	1.50
Amygdalar Complex	Amygdalar Complex	0.29	0.81	1.87	1.95
Entorhinal Ctx	Entorhinal Ctx	0.00	1.70	3.00	3.40
Pyriform Ctx	Pyriform Ctx	0.00	2.63	3.50	4.00
All Frontal Cortex	All Frontal Cortex	0.125	1.763	3.192	3.933

PRL Frontal Ctx	**Dorsolat Med Frontal Ctx (A9)**	0.13	1.76	3.19	3.93
IL/MO Frontal Ctx	**Middle Frontal Ctx (A46)**	0.13	1.88	3.25	3.93
Secondary Motor Ctx	**Secondary Motor Ctx (A6)**	0.12	1.64	3.13	3.93
Primary Motor Ctx	**Primary Motor Ctx (A4)**	0.25	2.23	2.72	3.29
Primary Sensory Ctx	**Primary Sensory Ctx (A3)**	0.26	2.23	2.52	3.21
Posterior Parietal Ctx	**Posterior Parietal Ctx (A7)**	0.58	1.95	2.50	2.87
Primary Auditory Ctx	**Primary Auditory Ctx (A41)**	0.10	1.88	2.50	3.20
Temporal Assoc Ctx	**Superior Temporal Ctx (A22)**	0.14	2.17	2.42	2.96
Primary Visual Cortex	**Primary Visual Ctx (A17)**	0.16	2.11	2.54	2.81
Insular Ctx	**Insular Ctx (A13-16)**	0.19	1.84	2.55	2.66
Cingulate Cortex	**Cingulate Cortex (A24)**	0.13	2.08	2.63	3.03
All Cerebral Cortex	**All Cerebral Cortex**	0.13	1.50	2.77	3.48
PRL Frontal Ctx L2/3	**A9 Layers 2/3**	0.05	2.80	3.63	3.95
PRL Frontal Ctx L4	**A9 Layer 4**	-	-	-	-
PRL Frontal Ctx L5	**A9 Layer 5**	0.28	1.43	3.00	3.90
PRL Frontal Ctx L6	**A9 Layer 6**	0.08	1.43	3.13	3.95
IL/MO Frontal Ctx L2/3	**A46 Layers 2/3**	0.03	2.63	3.53	3.95
IL/MO Frontal Ctx L4	**A46 Layer 4**	-	-	-	-
IL/MO Frontal Ctx L5	**A46 Layer 5**	0.26	1.23	2.88	3.90
IL/MO Frontal Ctx L6	**A46 Layer s6**	0.06	1.08	3.00	3.95
Secondary Motor Ctx L2/3	**A6 Layers 2/3**	0.11	2.63	3.30	3.70
Secondary Motor Ctx L4	**A6 Layer 4**	-	-	-	-
Secondary Motor Ctx L5	**A6 Layer 5**	0.55	1.50	1.55	2.55
Secondary Motor Ctx L6	**A6 Layer 6**	0.10	2.58	3.30	3.62
Primary Motor Ctx L2/3	**A4 Layers 2/3**	0.12	2.63	3.05	3.57
Primary Motor Ctx L4	**A4 Layer 4**	-	-	-	-
Primary Motor Ctx L5	**A4 Layer 5**	0.58	1.50	1.38	2.50
Primary Motor Ctx L6	**A4 Layer 6**	0.10	2.58	3.13	3.57
Primary Sensory Ctx L2/3	**A1-3 Layers 2/3**	0.05	2.63	3.13	3.42
Primary Sensory Ctx L4	**A1-3 Layer 4**	2.00	1.68	2.38	2.65
Primary Sensory Ctx L5	**A1-3 Layer 5**	0.25	0.88	1.38	1.98
Primary Sensory Ctx L6	**A1-3 Layer 6**	0.00	2.63	3.13	3.42
Posterior Parietal Ctx L2/3	**A7 Layers 2/3**	0.04	2.55	3.13	3.68
Posterior Parietal Ctx L4	**A7 Layer 4**	0.10	1.48	2.38	2.85
Posterior Parietal Ctx L5	**A7 Layer 5**	0.23	0.88	1.38	2.50
Posterior Parietal Ctx L6	**A7 Layer 6**	0.05	2.63	3.13	3.78
Primary Auditory Ctx L2/3	**A41 Layers 2/3**	0.03	2.90	3.13	3.58
Primary Auditory Ctx L4	**A41 Layer 4**	0.20	1.75	2.13	2.45

Primary Auditory Ctx L5	**A41 Layer 5**	0.28	1.13	1.13	2.03
Primary Auditory Ctx L6	**A41 Layer L6**	0.06	2.90	3.30	3.78
Temporal Assoc Ctx L2/3	**A22 Layers 2/3**	0.03	2.63	3.18	3.38
Temporal Assoc Ctx L4	**A22 Layer 4**	0.13	1.68	2.35	2.35
Temporal Assoc Ctx L5	**A22 Layer 5**	0.38	1.13	1.30	1.83
Temporal Assoc Ctx L6	**A22 Layer 6**	0.10	3.03	3.35	3.68
Primary Visual Ctx	**A17 Layers 2/3**	0.05	2.70	3.00	3.10
Primary Visual Ctx	**A17 Layer 4**	0.15	1.70	1.80	1.80
Primary Visual Ctx	**A17 Layer 5**	0.40	0.45	2.40	2.55
Primary Visual Ctx	**A17 Layer 6**	0.15	2.50	3.00	3.20
Insular Ctx L2/3	**A13-16 Layers 2/3**	0.38	0.63	2.13	2.75
Insular Ctx L4	**A13-16 Layer 4**	0.19	1.33	2.63	3.25
Insular Ctx L5	**A13-16 Layer 5**	0.13	0.38	0.85	1.00
Insular Ctx L6	**A13-16 Layer 6**	0.75	1.25	1.88	2.38
Thalamus	**Thalamus**	0.18	0.33	0.63	1.88
PFN of Thalamus	**PFN of Thalamus**	0.19	1.33	2.63	3.25
Hypothalamus	**Hypothalamus**	0.13	0.38	0.85	1.00
PVN of Hypothalamus	**PVN of Hypothalamus**	0.75	1.25	1.88	2.38
Subthalamic Nucleus	**Subthalamic Nucleus**	0.18	0.33	0.63	1.88

Table 4

		Q175	Q175	Q175 ISHH		HD Gr1 Count
SPN Type	**Q175 Age**	**Agg Area**	**Diffuse Area**	**% of Cntrl**	**SPN Type**	**% of Cntrl**
dSPN	**6 mo**	2.78%	7.64%	95.0%	**dSPN**	70.9%
iSPN	**6 mo**	2.47%	5.19%	84.7%	**iSPN**	33.6%
dSPN	**18 mo**	2.79%	1.72%	93.0%	**dSPN**	70.9%
iSPN	**18 mo**	3.11%	1.69%	74.5%	**iSPN**	33.6%

Table 5

	11G2	11G2	11G2	11G2	11G2
Brain	**Load**	**Load**	**Load**	**Load**	**Load**
Region	**Grade 0**	**Grade 1**	**Grade 2**	**Grade 3**	**Grade 4**
Caudate	-	1.10	1.60	1.50	1.38
Putamen	-	1.20	1.60	2.08	1.50
All Striatum	-	1.15	1.60	1.79	1.44
Accumbens	-	2.00	1.00	1.50	1.75
GPe	-	1.00	1.30	1.00	1.00
GPi	-	1.00	1.38	1.50	1.00
VP	-	-	1.00	2.00	1.00
SNr	1.50	1.25	1.40	2.00	1.25
Insular Ctx	-	1.75	2.00	1.87	1.67
A9	-	2.17	2.03	1.94	1.79
A46	-	1.92	1.97	1.92	1.67
A6	0.50	2.00	1.96	2.13	1.94
A4	-	1.75	1.79	1.67	1.69
A7	-	1.25	1.61	1.50	1.33
A22	1.33	1.50	1.53	1.92	1.46
Hp	0.00	0.00	1.40	1.00	0.67
Entorhin Ctx	0.50	1.50	2.00	2.00	1.38
A9 L2/3	-	2.00	2.00	2.00	1.50
A9 L4	-	2.00	1.83	1.50	1.38
A9 L5/6	-	2.50	2.25	2.33	2.50
A46 L2/3	-	1.75	2.00	2.00	1.25
A46 L4	-	1.75	1.75	1.50	1.25
A46 L5/6	-	2.25	2.17	2.25	2.50
A6 L2/3	0.00	1.50	1.83	1.75	1.63
A6 L4	-	-	-	-	-
A6 L5/6	1.00	2.50	2.08	2.50	2.25
A4 L2/3	-	1.25	1.67	1.50	1.38
A4 L4	-	-	-	-	-
A4 L5/6	-	2.25	1.92	1.83	2.00
A7 L2/3	-	1.00	1.83	1.75	1.25
A7 L4	-	1.00	1.00	1.00	1.00
A7 L5/6	-	1.75	2.00	1.75	1.75

A22 L2/3	1.50	1.50	1.67	2.26	1.50
A22 L4	1.00	1.50	1.17	1.50	1.00
A22 L5/6	1.50	1.50	1.75	2.00	1.88
Insular L2/3	-	1.63	1.90	2.00	1.25
Insular L4	-	1.50	1.70	1.10	1.25
Insular L5/6	-	2.13	2.40	2.50	2.50
CA1	0.00	0.00	1.40	1.00	0.67
CA2	0.00	0.00	1.40	1.00	0.67
CA3	0.00	0.00	1.40	1.00	0.67
CA4	0.00	0.00	1.40	1.00	0.67
Dentate	0.00	0.00	1.40	1.00	0.67
Dent Hilus	0.00	0.00	1.40	1.00	0.67
Subiculum	0.00	0.00	1.40	1.00	0.67
Thalamus	-	1.00	1.13	1.25	1.17